F. SUPPLEMENTARY MATERIAL — PART F

$\mathbf{Li^+}$–$\mathbf{H_2(D_2)}$

versus

$\mathbf{He}$–$\mathbf{H_2^+(D_2^+)}$

Fig. F1. Electronic structure input

to calculations on dynamics and spectroscopy of the systems

– the most important differences

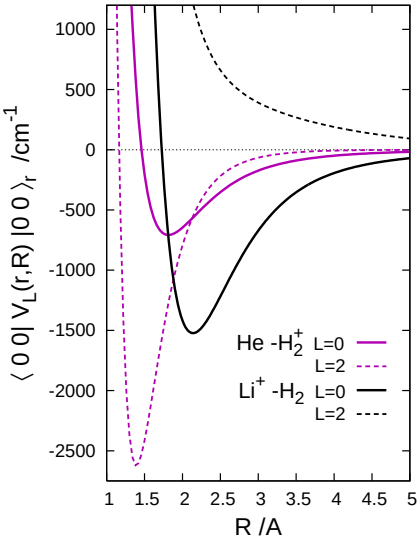

The PESes of the ground electronic states of $[LiHH]^+$ and $[HeHH]^+$, their Li^++HH and He+HH^+ arrangement valeys, the former as in the paper, the latter — taken from Ref. 1, referred to as PES02.

Fig. F1a. Two leading strength functions $V_L(r,R,\theta)$ of the interactions potentials $\overline{V}^{Li^+-HH}(r,R,\theta)$ and $\overline{V}^{He-HH^+}(r,R,\theta)$, defined as in Fig. E1 and

$$\overline{V}^{He-H_2^+}(r,R,\theta) - \overline{V}^{He-H_2^+}(r,R{\to}\infty) = \sum_{L=0}^{10} V_L^{He-H_2^+}(r,R)P_L(\cos\theta)\,,$$

averaged in the functions of v=0 j=0 states of the diatomic subunits. To note are the differences in the sign and size of L=2 terms.

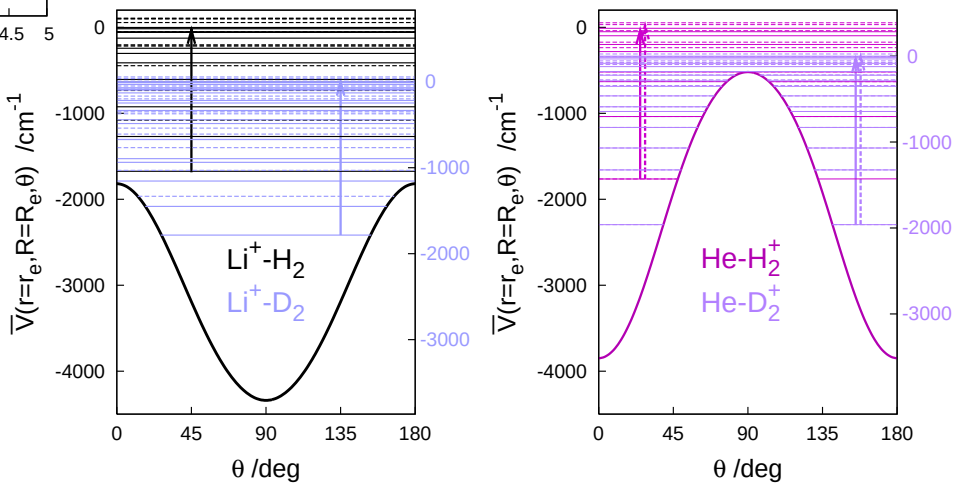

Fig. F1b. 1D cuts through the minima of the PESs and location of the J=0 bound state energy levels of the complexes Li^+-H_2 (D_2) and He-H_2^+ (D_2^+). Levels of the complexes formed with *ortho*-H_2 (-H_2^+) and *para*-D_2 (-D_2^+) are shown with dashed lines. The zeros of E in the right panel — the dissociation limits v=0 j=0 of He-*p*H_2^+ and He-*o*D_2^+ lying 3849.7 and 3514.8 cm^{-1}, respectively, above the minimum of $\overline{V}^{He-H_2^+}$ and 1147.0 and 812.1 cm^{-1} above the asymptote of this PES. The limits v=0 j=1 of He-*o*H_2^+ and He-*p*D_2^+ lie 58.22 and 29.33 cm^{-1}, respectively, higher. ZPE(He–a_2^+)=2086 (1553) cm^{-1} for a=H (D).

The components $d_Z(r,R,\theta)$ and $d_X(r,R,\theta)$ of the electric dipole vector fields of Li^+–H_2 and He–H_2^+; the analytical fits from Ref. 2 taken for the latter complex; the acronym DMS97 is used for them in further text.

Fig. F1c. Strength functions $D_{L|\Lambda|}(r,R)$ of the dipole components resulting from expansions in the Legendre functions $P_L^{|\Lambda|}(\cos\theta)$, matrix elements between $v\,j$ states of diatomic subunits. To note are the opposite signs of the elements $\langle 0|D_{00}|0\rangle$ in the two panels and the different relations $\langle\,|D_{21}|\,\rangle$:$\langle\,|D_{20}|\,\rangle$ at Rs around the R_es.

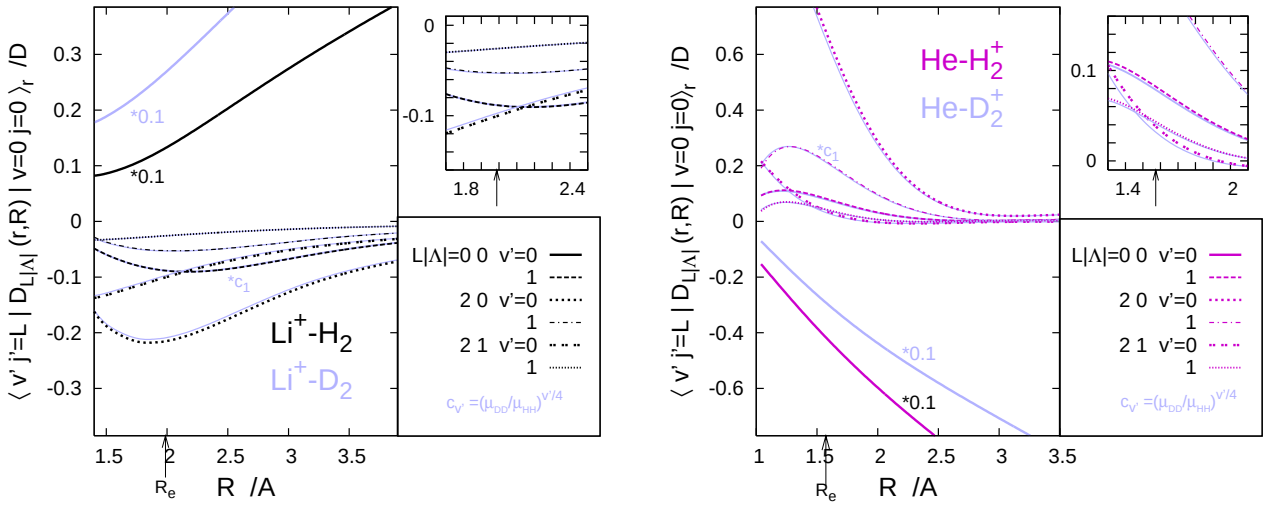

Fig. F2. Energies of 'vibrational' bound states of $He–H_2^+(D_2^+)$.

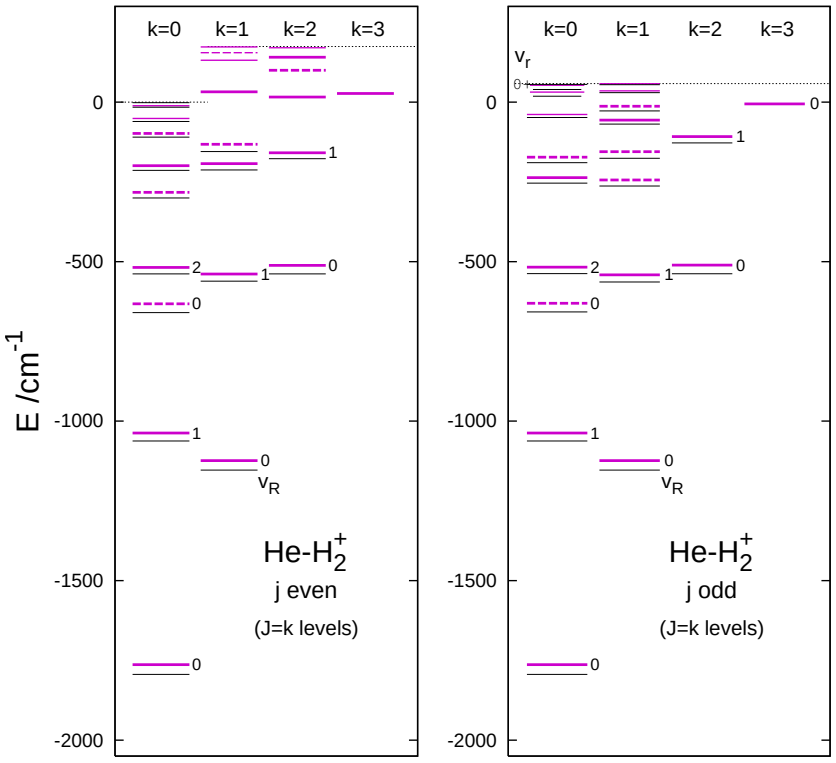

Fig. F2a. Energies $E([\mathrm{v}], k, J{=}k, p)$ of $He–H_2^+(I)$ for $I{=}0, 1$ in the ranges: $E{<}\varepsilon_{v=0\,j=0}$ for $I{=}0$ and $p{=}1$, $E{<}\varepsilon_{0\,2}$ for $I{=}0$, $p{=}{-}1$, and $E{<}\varepsilon_{0\,1}$ for $I{=}1$. The values resulting from the PES of Ref. 1, presented in Table II and Fig. 3 of Ref. 3, are compared here to the values from the newest PES (Ref. 4) presented in Table 1 of Ref. 5 (the violet versus black lines). The lines in $k{>}1$ columns, all such lines in the right panel and these lying below the threshold $\varepsilon_{0\,0}{=}0$ in the left panel, represent actually two energies, of states differing only in the parity p; the splitting between these energies is too small to be visible on the scale of the figure. Only f parity states of energies in the range $\varepsilon_{0\,0}$–$\varepsilon_{0\,2}$ are bound.

Because of smaller binding of the PES02 (by 32.4 cm^{-1} in the value of D_e) the energy levels generated from it lie higher than the levels from the PES of Ref. 4, later on referred to as PES19. The difference between the lowest levels (i.e. in the dissociation energy D_0) is 30.4 cm^{-1}. The number of $J{=}0$ bound states of each complex, with pH_2^+ and with oH_2^+, is smaller by one. The numbers of bound $J{=}k{=}1$ and $J{=}k{=}2$ states supported by both PESs appear the same, if not counting the states in the range $\varepsilon_{0\,0}$–$\varepsilon_{0\,2}$; they were not determined in Ref. 5. No energy level listed in Table 1 of that paper is assigned with $k{=}3$.

Results of the analyses performed in Refs. 1 and 3 in order to assign the states with vibrational quantum numbers are also partly displayed in the figure. The dashed lines show states assigned with $\widetilde{v}_\theta{>}0$. The two shorter continuous lines in $k{=}0$ column of the right panel mark states with increased excitation in the r-mode, see Fig. F6a.

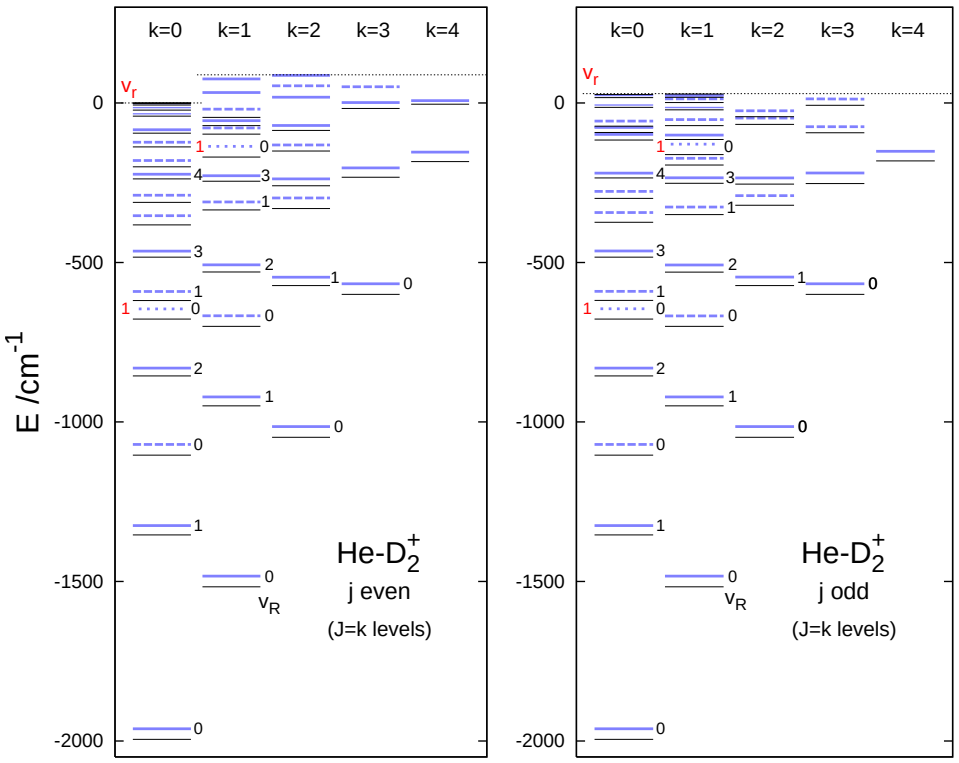

Fig. F2b. Same as Fig. F2a for $He–D_2^+$. Blue lines — energies from the PES02, listed in Table FI, black lines — energies from the PES19, listed in Table 2 of Ref. 5. Table FI contains also results of the natural expansion analysis of the functions of the states. Of these results shown are here: states assigned with $v_r{=}1$ — dotted lines, states excited in the θ-mode, in the majority assignable with $\widetilde{v}_\theta{=}2$ — dashed lines, and many assignments with the number v_R.

TABLE FI. Energies of 'vibrational' (J=k) bound states of He–D_2^+ from the PES02 (Ref. 1), calculated in this work. Comparison with the energies from the PES19 (Ref. 4), calculated in Ref. 5. Natural expansion analysis (NEA) of functions of the states[a] — assignment of quantum numbers.

		He–D_2^+ (I=0, 2)						He–D_2^+ (I=1)					
		$E([\mathrm{v}], k, J{=}k, p)$[b]				NEA[c]		$E([\mathrm{v}], k, J{=}k, p)$[b]				NEA[c]	
k	[v][d]	PES02	$e-f$	PES19	Δ	λ $[v_r \widetilde{v}_\theta v_R]$[e]	%	PES02	$e-f$	PES19	Δ	λ $[v_r \widetilde{v}_\theta v_R]$[e]	%
0	1	−1961.99		−1995.0221	33.0	0 [0 0 0]	99.8	−1961.99		−1995.0221	33.0	0 [0 0 0]	99.8
	2	−1325.03		−1354.0790	29.1	[0 0 1]	99.5	−1325.03		−1354.0790	29.1	[0 0 1]	99.5
	3	−1070.57		−1103.9373	33.4	[0 2 0]	93.1	−1070.57		−1103.9344	33.4	[0 2 0]	93.1
	4	−831.07		−855.4376	24.4	[0 0 2]	95.3	−831.07		−855.4350	24.4	[0 0 2]	95.3
	5	−645.64		−677.5048	31.9	[1 0 0]	83.8	−645.59		−677.4620	31.9	[1 0 0]	84.0
						[0 2 0]	12.0					[0 2 0]	12.2
	6	−591.32		−619.4238	28.1	[0 2 1]	*76.2	−590.86		−618.9803	28.1	[0 2 1]	76.4
						[1 0 0]	*10.4					[1 0 0]	9.1
	7	−464.43		−483.4875	19.1	[0 0 3]	90.8	−464.32		−483.3874	19.1	[0 0 3]	90.9
	8	−353.56		−382.0840	28.5	[0 4 0]	69.8	−343.66		−373.8092	30.1	[0 4 0]	72.5
						[0 0 2]	17.9					[0 2 2]	17.6
	9	−289.34		−311.6660	22.3	[0 2 1]	70.8	−277.37		−298.9760	21.6	[0 2 1]	71.7
						[0 6 0?]	16.8					[0 0?4]	14.1
												[0 6 0]	10.6
	10	−223.38		−238.0913	14.7	[0 0 4]	84.3	−220.05		−234.7883	14.7	[0 0 4]	83.2
												[0 2 3]	11.5
	11	−180.56		−199.9992	19.4	[0 4 2]	72.2	−98.87		−116.1312	17.3	[0 4?1]	39.8
						[0 2 3]	20.2					[0 2 5]	33.3
												[0 4 3]	22.7
	12	−123.01		−137.6518	14.6	[0 2 2]	72.3	−76.94		−92.6281	15.7	[0 0 4]	52.4
						[0 0?5]	14.4					[0 4 3]	35.8
	13	−84.08		−94.6518	10.6	[0 0 5]	78.5	−56.89		−72.7767	15.9	[0 2 3]	60.1
						[0 2 4]	13.7					[0 2 4]	18.7
												[0 4 0]	11.3
	14	−34.08		−41.4540	7.4	[0 0 6]	62.7	−6.40		−13.7453	7.3	[0 0 6]	91.5
						[0 2 5]	31.2						
	15	−14.78		−22.3532	7.6	[0 0?5]	62.2	23.15		16.6751	6.5	[0 0 7]	94.3
						[0 2 5]	26.5						
	16	−2.03		−6.2553	4.2	[0 0 6]	93.0			26.6910			
	17			−0.9668									
	18			−0.1169									
1	1	−1483.16	−0.13	−1516.5355	33.4	1 [0 0 0]	99.6	−1483.16	−0.13	−1516.5356	33.4	1 [0 0 0]	99.6
	2	−921.65	−0.20	−949.4136	27.8	[0 0 1]	97.3	−921.66	−0.20	−949.4194	27.8	[0 0 1]	97.3
	3	−667.39	−0.41	−700.2484	32.9	[0 2 0]	88.3	−667.56	−0.38	−700.3920	32.8	[0 2 0]	88.2
	4	−507.82	−0.36	−529.8007	22.0	[0 0 2]	90.1	−508.21	−0.30	−530.1651	22.0	[0 0 2]	89.8
	5	−310.63	−2.28	−335.1855	24.6	[0 2 1]	70.7	−326.33	1.30	−349.8114	23.5	[0 2 1]	74.0
						[0 0 3]	14.7					[0 0 3]	12.8
	6	−228.35	−2.22	−245.3216	17.0	[0 0 3]	84.0	−234.64	−0.57	−251.5912	16.9	[0 0 3]	80.5
						[0 2 2]	10.8					[0 4?1]	11.2
	7	−136.26	−0.06	−169.6786	33.4	[1 0 0]	*83.9	−173.47	−0.12	−194.5276	21.1	[0 4?1]	63.6
						[0 2 1]	*9.2					[0 4 3]	20.2
	8	−78.47	−0.12	−97.7063	19.2	[0 2 3]	46.1	−129.37	−0.24	−161.9222	32.6	[1 0 0]	*76.0
						[0 0 4]	35.3					[0 4 1]	*14.0
						[0 4 2]	14.4						
	9	−55.73	−0.23	−71.0678	15.3	[0 0 3]	65.2	−100.75	−0.56	−114.3652	13.6	[0 0 3?]	70.9
						[0 4 2]	26.1					[0 4 3]	20.2
	10	−19.62	−1.08	−45.0902	25.5	[0 4 1?]	68.2	−52.16	0.87	−70.8379	18.7	[0 4 2]	62.6
						[0 4 2?]	17.3					[0 2?2]	21.4
	11	32.45				[0 0 5]	92.4	−14.42	0.12	−21.5098	7.1	[0 0 5?]	76.9
												[0 2 4]	18.5

TABLE FII. continued

	12	75.41				[0 0 6]	96.1	12.77	0.11	1.1218	11.6	[0 2 5?]	50.0
												[0 0?4]	33.4
												[0 4 3]	14.2
	13							23.48	−0.13	17.6248	5.9	[0 0 5]	79.6
										27.8931			
2	1	−1014.64	0.00	−1048.2026	33.6	2 [0 0 0]	98.1	−1014.64	0.00	−1048.2014	33.6	2 [0 0 0]	98.1
	2	−546.30	0.00	−572.4646	26.2	2 [0 0 1]	89.2	−546.06	0.01	−572.2334	26.2	2 [0 0 1]	89.2
	3	−298.07	−0.71	−330.8432	32.8	2 [0 2 0]	60.9	−290.82	−0.06	−320.5937	29.8	2 [0 2 0]	74.2
						2 [0 0 2]	12.6					2 [0 2 2]	14.7
						1 [0 2 1]	12.8						
	4	−238.36	−0.40	−259.5189	21.2	2 [0 0 2?]	67.6	−235.06	−0.15	−254.4782	19.4	2 [0 0 2]	39.5
						2 [0 4 0?]	15.2					1 [0 0 3]	40.6
						1 [0 0 3]	10.1						
	5	−131.79	−0.01	−150.5633	18.8	2 [0 2 2]	70.3	−47.60	0.16	−67.2911	19.7	2 [0 2 2]	50.5
						2 [0 0 3]	16.7					2 [0 0 3]	38.5
	6	−70.85	−0.11	−86.1104	15.3	2 [0 0 2]	57.0	−24.90	0.08	−42.9583	18.1	2 [0 2 2]	61.0
						1 [0 0 4]	15.7					2 [0 4 0]	20.2
						1 [0 2 4]	11.2						
	7	18.06				2 [0 0 3]	83.4						
	8	53.82				2 [0 2 3]	63.6						
						2 [0 2?3]	20.5						
						2 [0 4 3]	10.2						
	9	86.51				2 [0 0 5]	94.0						
3	1	−567.21	−0.01	−599.8346	32.6	3 [0 0 0]	91.8	−567.25	−0.01	−599.8635	32.6	3 [0 0 0]	91.9
	2	−203.67	−2.81	−232.9096	29.2	3 [0 0 1]	34.7	−219.61	−1.10	−252.5279	32.9	3 [0 0 1]	56.2
						2 [0 0 2]	24.7					1 [0 0 3]	26.0
						1 [0 0 3]	23.8						
	3	1.14	0.73	−17.1834	18.3	3 [0 0 2]	*32.7	−74.55	0.00	−93.5988	19.0	3 [0 2 1]	69.0
						3 [0 2 1]	*13.6					3 [0 0 2]	24.8
						1 [0 4 1]	*28.1					3 [0 4 1]	10.5
						2 [0 0 2]	*10.6						
	4	50.55				3 [0 2 1]	65.3	12.81	0.00	−7.2595	20.1	3 [0 2 1]	73.1
						3 [0 4?1]	19.0					3 [0 4?1]	18.8
4	1	−154.50	0.00	−183.8870	29.4	4 [0 0 0]	89.7	−151.95	0.00	−181.7481	29.8	4 [0 0 0]	91.1
	2	7.01		−3.8015	10.8	4 [0 0 1]	78.0						
						4 [0 2 1?]	11.9						

[a] The version of the analysis described in Ref. 3. See also the description at the end of this material, Eqs. (F1)–(F20), and Fig. F6.

[b] Energies of f-parity states are listed in columns 'PES02' and 'PES19' when k>0.

'$e-f$' — the energy splitting between e- and f-parity states from the PES02 (if both states are bound).

Δ:=E(PES02) − E(PES19).

[c] For each state of the energy listed in column 'PES02', the following information is presented on the configurations of the three natural orbitals, in the r-, θ-, and R-coordinate, in terms of which the λ components of the total function of the state can be expanded:

1) the λ of the component in which the configuration occurs,

2) the quantum numbers assigned to the orbitals in the configuration (note that $\widetilde{v}_\theta$=v_θ−1 and $\widetilde{v}_\theta$=v_θ for λ+I odd and even, respectively, where v_θ is the number used for the Li^+–H_2 (D_2) complexes), and

3) the occupancy of the configuration in the total function.

All configurations with the occupancy larger than 10% are shown for each state analyzed. The asterisk in front of the occupancy listed in column '%' is to notify that orbitals forming the respective configuration are plotted in Fig. F6.

[d] Formal label of states assigned with given k; may be replaced with the numbers $[v_r\,\widetilde{v}_\theta\,v_R]$ of the most populated natural configuration, if the population is above 50%.

[e] Related to the customary label of states of linear complexes with strong anisotropy[6], $[v_r\,v_b^\lambda\,v_R]$, as: v_b=$\widetilde{v}_\theta$+λ.

COMMENTS

(i). The consequences of the differences in the electronic structure input exposed in Fig. F1 for the comparison of dynamics of the two pairs of atom-diatom ionic complexes are qualitatively the same as those displayed in Refs. 3 and 7 in the comparison of the $He^+ + H_2$ and $He + H_2^+$ systems in their free, quasi-bound and states (being important in the initial, intermediate, and final channels of the radiative charge transfer and radiative association reactions studied there). These consequences are: a) different patterns of vibration-rotation energy levels of bound and quasi-bound states (demonstrated also in the present material: Fig. F2 versus Fig. E2 in Part E), b) disparate sizes of λ-, j-, and v-mixing in the functions of all kinds of the states, c) disparate rates of dissociative decay of the resonance states, especially of the decay by vibrational predissociation mechanism. The consequences for the absorption spectra of the differences in the DMSs seen in Fig. F1c, in the first place, but also of the differences named in point b), will be one of main themes in this material.

(ii). The material enclosed here has essentially two goals. Both refer to the content of Sec. IVD of the paper, specifically: a) to the statement that the presented new results on vibrational band intensities of the absorption spectra of the Li^+–H_2 (D_2) complexes are even qualitatively dissimilar to the results reported in Ref. 8, and b) to the (initially unexpected) finding on the combination bands v_r=0→1+v_θ=0→1 and v_r=0→1+v_R=0→1 in the spectra of both complexes: the former are nearly 100 times more intense than the latter and only about 15 times less intense than the v_r fundamental bands. The dominant role in building the intensities of the v_r=0→1 + v_θ=0→1 bands is played by the smaller of the two components of the dipole moment vector in the BF-reference frame specified in the paper (Sec. II), i.e. by the component d_X, along the axis in the three-nuclei plane perpendicular to the atom-diatom axis Z.

The goals are:

(1) to provide further evidence of correctness of the procedures used in the intensity calculations. The evidence provided in Part C (Table CXVIII) concerns only a-type bands. Making sure that the procedures worked correctly also in application to b-type bands is desirable as this will increase the credibility of the potentially useful finding iib.

(2) to inspect the impact of the d_X dipole component on the strengths of photo-transitions in the He–H_2^+ and He–D_2^+ complexes. The component was accounted for in the calculations of rotation-vibration linestrenghts for HeH_2^+ reported in Refs. 2 and 9. Preasumably, its contributions were found small in these calculations but none details/comments were given on this point. In the calculations of the DMSs that accompanied the generation of the refined PES02[1] for the ground electronic states of HeH_2^+ and of the PES for the first excited state, only the d_Z components were determined[10]. Thus, in the subsequent calculations on the radiative reactions[3, 7, 11] for which these PESs and DMSs were actually prepared, in particular, in the calculations on the radiative association in the $He + H_2^+$ collisions, the component d_X was assumed unimportant. Providing some information supporting/verifying this assumption seems a proper thing to do here, on the occassion of reporting on the definitely non-negligible impact of the d_X on the absorption spectra of the Li^+–H_2 and Li^+–D_2 complexes.

Fig. F3. Line strengths*

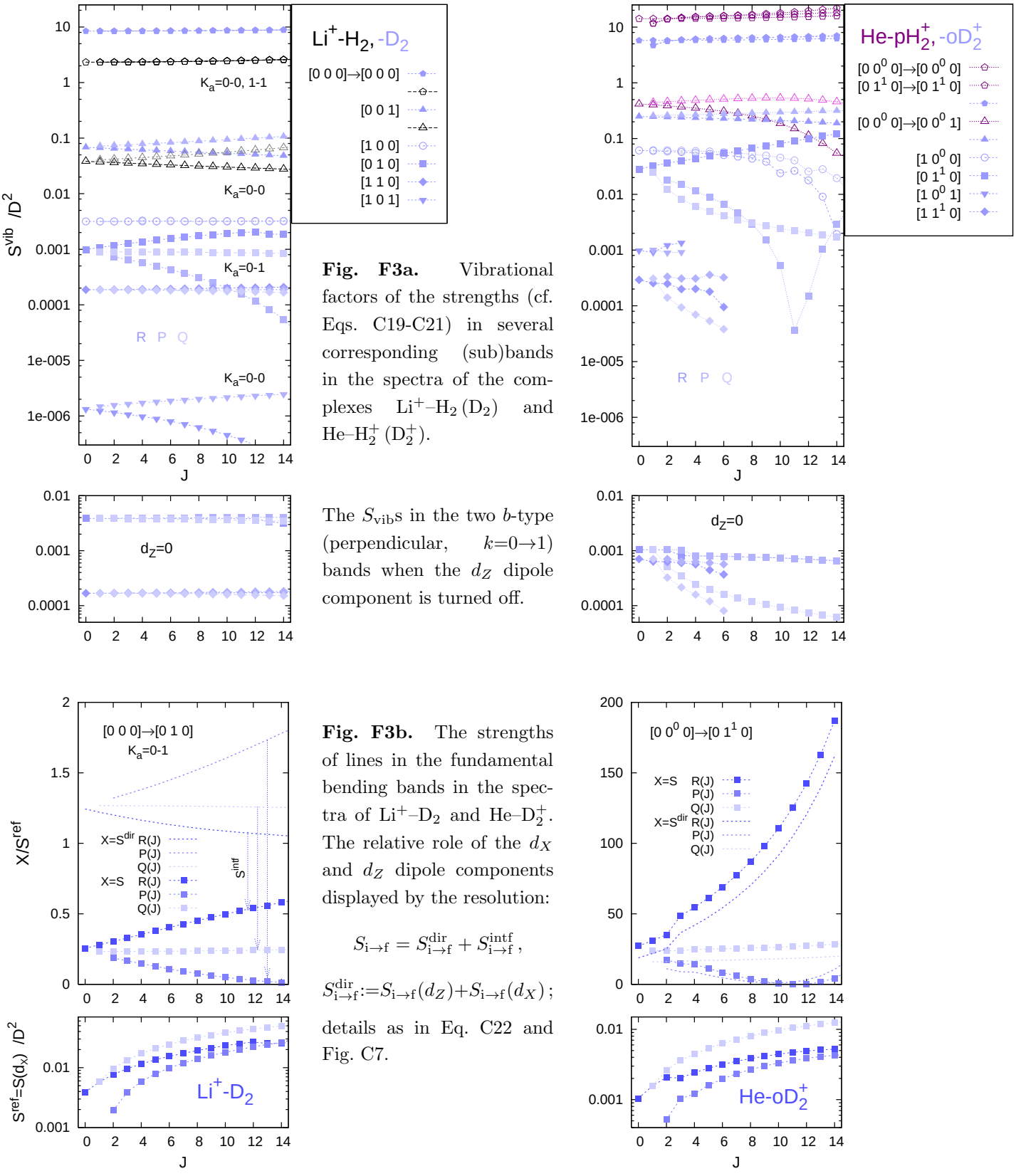

Fig. F3a. Vibrational factors of the strengths (cf. Eqs. C19-C21) in several corresponding (sub)bands in the spectra of the complexes Li^+–H_2 (D_2) and He–H_2^+ (D_2^+).

The S_{vib}s in the two b-type (perpendicular, k=0→1) bands when the d_Z dipole component is turned off.

Fig. F3b. The strengths of lines in the fundamental bending bands in the spectra of Li^+–D_2 and He–D_2^+. The relative role of the d_X and d_Z dipole components displayed by the resolution:

$$S_{i\to f} = S^{dir}_{i\to f} + S^{intf}_{i\to f},$$

$$S^{dir}_{i\to f} := S_{i\to f}(d_Z) + S_{i\to f}(d_X);$$

details as in Eq. C22 and Fig. C7.

* The accuracy of the line strengths presented here for He–H_2^+ (D_2^+) is documented in Tables FIII and FIV by comparison with the strengths obtained in Ref. 5 from the newest electronic structure data.

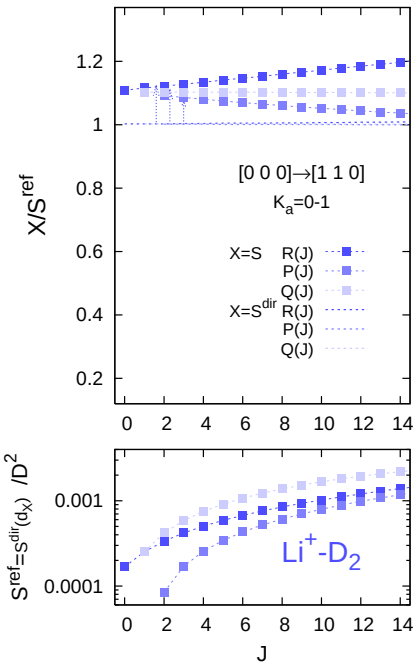

Fig. F3c.
Same as Fig. F3b for the combination bands: v_r=0→1 plus v_θ=0→1 or v_b=0→1.

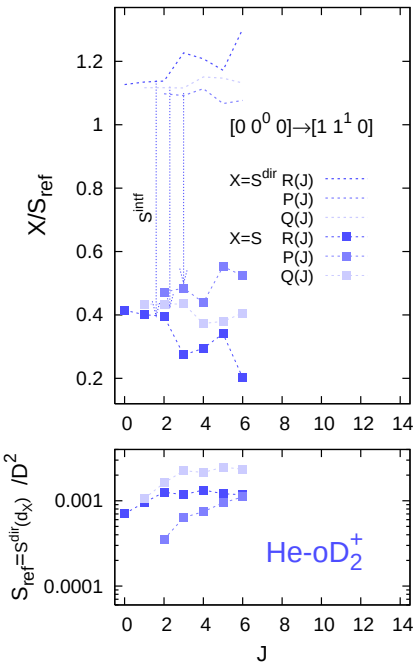

TABLE F3s. Supplementary information on the strengths of $R(0)$ lines[a] in four of the vibrational (sub)bands of the Li^+–D_2 and He–oD_2^+ complexes shown in Figs. F3a-c (on contributions of different parts of the DMSs, on interference between transition amplitudes mediated by these parts, on the role of λ-mixing in final states of the transitions.)

[0] 0 →[v′] k′	S [b]	$S^{\rm dir}$ [c]	$L\,\lvert\Lambda\rvert$	$S(\propto D_{L\lvert\Lambda\rvert})$ [d]	$\mathcal{D}^{L\lvert\Lambda\rvert}$ [e]	$\mathcal{P}^{L\lvert\Lambda\rvert}$ [f]	$\mathcal{S}^{L\lvert\Lambda\rvert}$ [g]
			Li^+–D_2				
[0 1 0] 1	9.888 (−4)	4.774 (−3)	2 1	3.856 (−3)	9.454 (−3)	0.788	
			0 0	9.174 (−4)	7.192	0.254 (−3)	
			21/00	*4.20*	*1.314 (-3)*	*3.102 (+3)*	*4.1*
[1 1 0] 1	1.866 (−4)	1.689 (−4)	2 1	1.682 (−4)	4.760 (−4)	0.762	
			0 0	6.535 (−7)	5.517 (−3)	0.267 (−3)	
			21/00	*257*	*8.628 (-2)*	*2.854 (+3)*	*246*
[0 0 1] 0	6.829 (−2)	7.175 (−2)	0 0	7.171 (−2)			
			2 0	3.772 (−5)			
[1 0 0] 0	3.166 (−3)	6.090 (−3)	0 0	5.721 (−3)			
			2 0	3.689 (−4)			
			He–oD_2				
[0 1^1 0]	2.836 (−2)	2.760 (−2)	2 1	8.206 (−4)	1.043 (−3)	0.672	
			0 0	2.617 (−2)	8.444	0.175 (−2)	
			21/00	*0.031*	*1.235 (-4)*	*3.840 (+2)*	*0.047*
[1 1^1 0]	2.927 (−4)	6.262 (−4)	2 1	5.592 (−4)	1.213 (−3)	0.621	
			2 0	5.549 (−5)	3.226 (−2)	0.582 (−2)	
			21/20	*10.1*	*3.760 (-2)*	*1.069 (+2)*	*4.0*
[0 0^0 1]	2.491 (−1)	1.635 (−1)	0 0	1.513 (−1)			
			2 0	1.220 (−2)			
[1 0^0 0]	6.118 (−2)	3.257 (−2)	2 0	2.777 (−2)			
			0 0	4.669 (−3)			

[a] Their values serve as the strengths of the entire bands, see Table XII. [b] Given in D^2. The contribution of the interference mentioned in the caption is $S^{\rm dir}-S$. [c] The 'direct' contribution defined as: $\sum_{L|\Lambda|} S(\propto D_{L|\Lambda|})$. [d] $S(\propto D_{L|\Lambda|})$ — the strength obtained using only the part $D_{L|\Lambda|}(r,R)\,P_L^{|\Lambda|}(\cos\theta)$ of the respective DMS. For each band, listed are the two largest $S(\propto D_{L|\Lambda|})$s; their $L\,|\Lambda|$ indices are in the preceding column. [e] Denotes: $|\langle 0|D_{L|\Lambda|}|v'{=}v_r\rangle_r|^2$ at $R{=}R_e$. The values of the matrix elements are taken from Fig. F1c. [f] Defined in Eq. (F1). Here it is the double sum: $\sum_j \sum_{j'=|j-L|,\geq|\Lambda|}^{j+L} \rho_{j\,0}\times\rho'_{j',\lambda'=|\Lambda|}$ where $\rho_{j\,0}$ and $\rho'_{j'\,\lambda'}$ are the populations plotted in Fig. F3s. [g] Denotes the product $\mathcal{D}^{L|\Lambda|}\times\mathcal{P}^{L|\Lambda|}$. Serves only an approximation of the ratio of the two largest $S(\propto D_{L|\Lambda|})$s in the k=0−1 subbands.

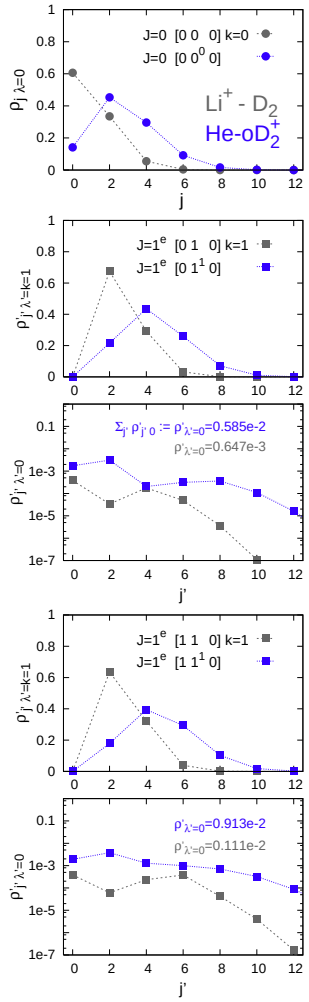

Fig. F3s. Population of $j\,\lambda$ states of oD_2 and oD_2^+ in the states of the complexes with Li^+ and He, respectively, specified in the legends (the initial and final states of $R(0)$ lines in the k=0−1 subbands of the b-type/perpendicular bands considered in Table F3s).

COMMENTS

(i). The following facts emerge from the comparison of line strengths in the two upper panels of Fig. F3a:

(i1) the H→D substitution in He–H_2^+ and in Li^+–H_2 have opposite impact (a decrease versus an increase) on the strengths of the purely rotational and the fundamental intermolecular stretching bands,

(i2) the $S^{\rm vib}$s of $R(J)$, $P(J)$, and $Q(J)$ lines in the nominally perpendicular $[0\,0^0\,0]\rightarrow[0\,1^1\,0]$ subband of He–oD_2^+ vary more strongly with growing J than the $S^{\rm vib}$s in the corresponding K_a=0−1 subband of the b type band $[0\,0\,0]\rightarrow[0\,1\,0]$ of Li^+–D_2,

(i3) the gap between the strengths in the two vibrational (sub)bands $[0\,0^0\,0]\rightarrow[0\,0^0\,1]$ and $[0\,0^0\,0]\rightarrow[0\,1^1\,0]$ of He–D_2^+ is several times smaller (∼7 times for low J lines) than the gap between the strengths in the corresponding subbands of Li^+–D_2,

(i4) the gap between the strengths in the fundamental diatomic stretching band $[0\,0^0\,0]\rightarrow[1\,0^0\,0]$ and in the combination band $[0\,0^0\,0]\rightarrow[1\,1^1\,0]$ of the NIR spectrum of He–oD_2^+ is larger, in turn, above 10 times, than the respective gap in the spectrum of Li^+–D_2,

(i5) the strengths of the seven lines determined in the parallel combination subband $[0\,0^0\,0]\rightarrow[1\,0^0\,1]$ of He–D_2^+ appear clearly larger (about 3 times) than the strengths in the perpendicular subband $[0\,0^0\,0]\rightarrow[1\,1^1\,0]$, contrasting with the relation between the respective subbands of Li^+–D_2 (the strengths in $[0\,0\,0]\rightarrow[1\,0\,1]$ K_a=0−0 overwhelmed by above two orders of magnitude by the strenghs in $[0\,0\,0]\rightarrow[1\,1\,0]$ K_a=0−1.)

(ii). For rationalization of the above facts, it is helpful to look at the following two resolutions of the strengths $S_{\rm i\rightarrow f}$ into 'direct' and 'interference' parts: 1) the resolution introduced in Eq. (C21), with the 'direct' part defined as the sum of the strengths $S_{\rm i\rightarrow f}(d_Z)$ and $S_{\rm i\rightarrow f}(d_X)$, each accounting only for the one indicated dipole moment component, and 2) a more detailed resolution, sensitive to the θ-dependence of the dipole components, with the direct part defined as $\sum_L \sum_{|\Lambda|=0,1} S_{\rm i\rightarrow f}(\propto D_{L|\Lambda|})$, where the strength $S_{\rm i\rightarrow f}(\propto D_{L|\Lambda|})$ accounts only for the term $D_{L|\Lambda|}(r,R)\,P_L^{|\Lambda|}(\cos\,\theta)$ of the component function $d_Z(r,R,\theta)$ when $|\Lambda|$=0 and $d_X(r,R,\theta)$ when $|\Lambda|$=1.

re (i1). In bands $[0\,0\,0]\rightarrow[0\,0\,0]$ and $[0\,0\,0]\rightarrow[0\,0\,1]$ of the spectra of all the four complexes considered, the line strengths $S_{\rm i\rightarrow f}$ (with d_Z and d_X included) are almost identical to the strengths $S_{\rm i\rightarrow f}(d_Z)$ and the latter are dominated by the $S_{\rm i\rightarrow f}(\propto D_{0\,0})$. Even more precisely, the size of $|\langle 0|D_{00}(r,R)|0\rangle_r|$ —the average in v=0 state of the respective diatomic subunit — is decisive. The size of $|\langle 0|D_{00}(r,R)|0\rangle_r|$ decreases upon the H→D substitution in He–H_2^+ (the center-of-mass of the complex shifts towards the location of the charge) and increases upon the substitution in Li^+–H_2.

re (i3). Unlike the strengths in the b-type bands of Li^+–H_2 (D_2), the line strengths in the perpendicular subbands $[0\,0^0\,0]\rightarrow[0\,1^1\,0]$ (also in the higher $[0\,1^1\,0]\rightarrow[0\,2^2\,0]$) of He–$H_2^+$ (D_2^+) are primarily determined by the component d_Z. For the deuterated complexes, this is evidenced in Fig. F3b by the ratios $S^{\rm dir}/S^{\rm ref}$=1+$S(d_Z)/S(d_X)$ being <2 and ≫2 in the left and right panel, respectively. Thus, the line strengths in the subband $[0\,0^0\,0]\rightarrow[0\,1^1\,0]$ of He–D_2^+ depend essentially on the same large dipole factor $|\langle 0|D_{00}(r,R)|0\rangle_r|$ as the strengths in $[0\,0^0\,0]\rightarrow[0\,1^1\,0]$. This may be at least a rough explanation of the smaller differences between these strengths as compared to the differences between their analogs in Li^+–D_2.

re (i2). The definition of $S^{\rm vib}_{\rm i\rightarrow f}$s, see Eqs. (C18)–(C20), is adjusted to the change of the number k ascribed to states 'i' and 'f' of transitions in a semi-rigid top. The component d_Z can have an impact on the strength of transition with $\Delta k\neq 0$ iff there is a λ-mixing in at least one 'i' or 'f' state. The larger the mixing is the more probable the transitions preserving the λ-value of the components of the states are. Obviously, the existence of substantial λ-mixing, ro-vibrational interactions, lowers the adequacy of the semi-rigid top model. This explains the observed increased variation of the $S^{\rm vib}$s with growing number J of lines in $[0\,0^0\,0]\rightarrow[0\,1^1\,0]$.

re (i4). In the perpendicular subband $[0\,0^0\,0]\rightarrow[1\,1^1\,0]$ of He–D_2^+, the component d_X acquires its nominal, i.e. leading, role. This is shown in Fig. F3c by the ratios $S^{\rm dir}/S^{\rm ref}$ in the right panel being similar to these in the left panel, i.e. <2.

re (i3)–(i4). The question arises: what lies at the bottom of the different relative roles of the components d_X and d_Z in building line strengths in the different considered $\Delta k\neq 0$ subbands. Based on the content of Table F3s, one may answer that this is an interplay between the two factors: (a) the size of the matrix element $\langle 0|D_{21}(R,r)|v{=}v_r\rangle_r$ relative to the size of the largest element $\langle 0|D_{L0}(R,r)|v{=}v_r\rangle_r$, and (b) the size of the λ-mixing in the initial and final states of transitions in the subbands. Strictly speaking, these factors determine relations between the strengths $S_{\rm i\rightarrow f}(\propto D_{21})$ and $S_{\rm i\rightarrow f}(\propto D_{L0})$ and do this in an 'entangled' way. In Table F3s, they are presented separately, by the italic numbers in columns '$\mathcal{D}^{L|\Lambda|}$' and '$\mathcal{P}^{L|\Lambda|}$', what was made possible by exploiting the following crude approximation:

$$S_{\rm i\rightarrow f}(\propto D_{L|\Lambda|}) \;\sim\; \underbrace{|\langle v{=}v_r|D_{L|\Lambda|}(R{=}R_{\rm e},r)|v{=}v'_r\rangle_r|^2}_{\mathcal{D}^{L|\lambda|}_{\rm i\rightarrow f}} \times \underbrace{\sum_{j,\lambda}\sum_{j',\lambda'}\rho^{\rm f}_{j'\lambda'}\,Z^{J_{\rm f}p_{\rm f},J_{\rm i}p_{\rm i}}_{L|\Lambda|}(j'\lambda',j\lambda)\,\rho^{\rm i}_{j\lambda}}_{\mathcal{P}^{L|\Lambda|}_{\rm i\rightarrow f}}$$
$$\sim \sum_{\lambda}\sum_{j\geq\lambda}\sum_{\lambda'=\lambda\pm|\Lambda|}\sum_{j'=|j-L|,\,\geq\lambda'}^{j+\lambda}\rho^{\rm f}_{j'\lambda'}\,\rho^{\rm i}_{j\lambda}\,, \quad \text{(F1)}$$

where $R_{\rm e}$ is the coordinate of the minimum of the respective PES (see Fig. F1c), $Z^{J_{\rm f}p_{\rm f},J_{\rm i}p_{\rm i}}_{L|\Lambda|}(j'\lambda',j\lambda)$ stands for the rotational coefficients which arise in the expression for the matrix element $\left[{}_{\rm BF}\mathbf{d}^{J_{\rm f}p_{\rm f},J_{\rm i}p_{\rm i}}(R)\right]_{v'j'\lambda',\,vj\lambda}$, Eqs. (21)–(24), when reorganized to the form $\sum_L\sum_{|\Lambda|=0,1}\langle v'j'|D_{L|\Lambda|}(r,R)|vj\rangle_r\,Z^{J_{\rm f}p_{\rm f},J_{\rm i}p_{\rm i}}_{L|\Lambda|}(j'\lambda',j\lambda)$, all non-zero values of these coefficients are set to 1 here, $\rho^{\rm f}_{j'\lambda'}$ is the population of state $j'\lambda'$ of diatomic subunit in state 'f' of the complex, and $\rho^{\rm i}_{j\lambda}$ is the analogous population in state 'i'.

In Table F3s listed are values of the two underbraced factors of expression (F1) for the two largest strengths $S(\propto D_{L|\Lambda|})$ of transitions i=$[0\,0\,0]J{=}0\rightarrow$ f=$[v'_r\,1\,0]J^e{=}k{=}1$ with $v'_r{=}0,1$ in Li^+-D_2 and He–D_2^+. In the transitions to states $[0\,1\,0]$, the strengths $S(\propto D_{2\,1})$ and $S(\propto D_{0\,0})$ are the two largest ones but opposite relations occur between them in the two complexes:

$$\frac{S(\propto D_{2\,1})}{S(\propto D_{0\,0})} \;\approx\; \frac{\mathcal{D}^{2\,1}}{\mathcal{D}^{0\,0}}\times\frac{\mathcal{P}^{2\,1}}{\mathcal{P}^{0\,0}}=0.001314\times 3102\;>1 \qquad \text{in } Li^+\text{–}D_2,$$
$$\sim \qquad 0.000123\times 384.0\ll 1 \qquad \text{in He–}D_2^+. \quad \text{(F2)}$$

The substantial decrease of the ratio $\frac{S(\propto D_{2\,1})}{S(\propto D_{0\,0})}$ in He–D_2^+ results from both the smaller size of d_X relative to d_Z (to the $\propto D_{0\,0}$ part of it) and the larger λ-mixing in the final state reflected here by the smaller value of $\frac{\mathcal{P}^{2\,1}}{\mathcal{P}^{0\,0}}$. The respective ratios to inspect for the transitions to states $[1\,1\,0]$ are: $\frac{S(\propto D_{2\,1})}{S(\propto D_{0\,0})}$ in Li^+-D_2 and $\frac{S(\propto D_{2\,1})}{S(\propto D_{2\,0})}$ in He–D_2^+. These ratios are substantially larger than ratios (F2), both are >1. This is almost entirely due to the changed relations between the involved dipole-moment related factors, i.e. due to the values of $\frac{\mathcal{D}^{2\,1}}{\mathcal{D}^{0\,0}}$ and $\frac{\mathcal{D}^{2\,1}}{\mathcal{D}^{2\,0}}$ being much larger than their analogs in the transitions to $[0\,1\,0]$.

It remains to estimate how much the interference between the different terms $\propto D_{L\,|\Lambda|}$ of the DMSs contributes to the comparison of the strengths $S_{\rm i\rightarrow f}$ in the four considered subbands of the two complexes. The juxtaposition of the values of S and $S^{\rm dir}$ in Table F3s, also for the two $\Delta k{=}0$ transitions, to states f=$[0\,0\,1]k{=}0J^e{=}1$ and $[1\,0\,0]01^e$, serves this purpose. One finds out that the gap between the subbands $[1\,1^1\,0]$ and $[1\,0^0\,0]$ of He–oD_2^+ would be about four times smaller if the interference did not exist. In the corresponding subbands of Li^+–D_2 the interference 'acts' reversely, as seen in Figs. F3b and F3c. The estimate from Table F3s — $\frac{S([1\,0\,0]\,0)}{S([1\,1\,0]\,1)}{=}0.47\frac{S^{\rm dir}([1\,0\,0]0)}{S^{\rm dir}([1\,1\,0]1)}$: the gap between these subbands would be about two times larger if it were determined by the $S^{\rm dir}$s. Thus, fact (i4) appears largely created (in $\sim$85 %) by the interference.

Vibrational band intensities

TABLE FII. Vibrational band origins ($\nu_{[v'']\to[v']}$), strengths ($S_{[v'']\to[v']}$), and intensities $I_{[v'']\to[v']}(T)$ at T=15K for several [v'']=[0 0 0]→[v'] bands. The units are: cm^{-1}, D^2, and cm/molecule, respectively. δI — relative percentage deviation of the $I_{[v'']\to[v']}$ from the value obtained using the energies and line strengths calculated in Ref. 5. The entries within slashes show effects of omission of d_X dipole component on the strengths and intensities of the perpendicular bands.

Li^+–H_2				He–H_2^+				
[v']	$\nu_{[v'']\to[v']}$ [a]	$S_{[v'']\to[v']}$ [a]	$I_{[v'']\to[v']}$ [b] ♠	[v']	$\nu_{[v'']\to[v']}$ [c]	$S_{[v'']\to[v']}$ [d]	$I_{[v'']\to[v']}$ [e] ♠	δI [f]
[0 0 1]	405.1	3.83 (−2)	6.54 (−18)	[0 0^0 1]	726.3	4.17 (−1)	1.24 (−16)	−3
[0 1 0]	594.3	3.28 (−3)	9.43 (−19)	[0 1^1 0]	639.5	6.36 (−2)	1.68 (−17)	3
		/1.76 (−4)/	/5.20 (−20)/			/4.50 (−2)/	/1.20 (−17)/	
[0 0 2]	750.4	8.66 (−4)	2.73 (−19)	[0 0^0 2]	1245.7	4.21 (−2)	2.07 (−17)	−5
[0 2 0]	1068.2	1.37 (−3)	6.06 (−19)	[0 2^0 0]	1132.2	1.24 (−3)	5.48 (−19)	−30
[1 0 0]	4053.1	4.73 (−3)	8.00 (−18)	[1 0^0 0]	1836.5	3.82 (−2)	2.72 (−17)	8 [g]
[1 0 1]	4463.6	2.40 (−6)	4.40 (−21)					
[1 1 0]	4658.5	3.25 (−4)	6.40 (−19)					
		/8.27 (−7)/	/1.71 (−21)/					
Li^+–D_2				He–D_2^+				
[0 0 1]	333.1	6.83 (−2)	9.55 (−18)	[0 0^0 1]	637.0	2.49 (−1)	6.55 (−17)	−4
[0 1 0]	451.3	9.89 (−4)	2.04 (−19)	[0 1^1 0]	478.7	2.84 (−2)	5.62 (−18)	3
		/9.37 (−4)/	/1.95 (−19)/			/1.85 (−2)/	/3.69 (−18)/	
[0 0 2]	629.3	1.32 (−3)	3.49 (−19)	[0 0^0 2]	1130.9	1.36 (−2)	6.39 (−18)	−1
[0 2 0]	846.2	1.06 (−3)	3.71 (−19)	[0 2^0 0]	891.4	9.09 (−3)	3.32 (−18)	−5
[1 0 0]	2915.4	3.17 (−3)	3.85 (−18)	[1 0^0 0]	1316.4	6.13 (−2)	3.28 (−17)	−5
[1 0 1]	3251.3	1.32 (−6)	1.78 (−21)	[1 0^0 1]	2030.7	8.76 (−4)	7.97 (−19)	[h]
[1 1 0]	3371.1	1.87 (−4)	2.64 (−19)	[1 1^1 0]	1829.0	2.82 (−4)	2.05 (−19)	39
		/4.78 (−7)/	/6.89 (−22)/			/8.53 (−5)/	/6.36 (−20)/	

[a] Defined in Table XII of the paper. [b] Together with the values for T=296 K in Table XII, these data illustrate numerically the temperature dependence of the integrated intensities of the bands starting from the ground state [0 0 0] which is seen in Figs. C9 and F4. [c] The origin of band [0 0^0 0]→[v_r v_b^k v_R] is: $\big[E([v_r\, v_b^k\, v_R], J^p{=}k^e) - E([0\,0^0\,0], J{=}0)\big]/hc$. The origins of identically assigned bands in the spectra of the complexes with para- and ortho- H_2^+ (D_2^+) are in some cases clearly separated, see Table FV. The averages of their positions are given here. [d] Taken as the average of the strengths of $R(0)$ lines in the bands pertaining to the complexes with para- and ortho- H_2^+ (D_2^+). [e] The sums of the intensities of lines $R(J)$, $P(J)$, and $Q(J)$ for $J{\le}2$ and $J{\le}3$ in the bands of He–H_2^+ and He–D_2^+, respectively, which are listed in Tables FVI–FVII, in their 'PES02+DMS97' columns. The values of $I_{[v'']\to[v']}$ give the areas of the peaks in the absorption cross-sections $\sigma(\nu; T{=}15\,\mathrm{K})$ of the complexes plotted in Fig. F5 (with the violet and blue lines). [f] The deviations of the individual line intensities summed up in each $I_{[v'']\to[v']}$ listed here can be found in Tables FVI–FVII. [g] The I of Ref. 5 for [v']=[1 0^0 0] includes lines of He–oH_2^+ only. [h] The final states of all transitions in the band are resonances, not determined in Ref. 5.

COMMENTS

♠ The approximation introduced in Part C, Eq. (C23), may be applied here as $4.162379{\times}10^{-19}{\times}\nu_{[v'']\to[v']}{\times}S_{[v'']\to[v']}$ because the population factor takes values very close to 1 at T=15 K. The deviations $|I^{\mathrm{appr}}/I{-}1|$ are below 5 % for the majority of the bands shown. Obviously, this does not necessarily imply that the approximation is good at higher Ts. Several examples in Fig. C9 testify to this truth. In Fig. F4, the temperature dependence of the intensity $I_{[0\,0\,0]\to[0\,1\,0]}$ of He–H_2^+ is shown to differ qualitatively from the dependence encoded in formula (C23), importantly, for reason not occurring in Li^+–H_2 (D_2). See comments 're (i3)' and 're (i3)–(i4)'.

The impact of the dipole component d_X on the relative intensities of the vibrational bands in the absorption spectra of the He–H_2^+ (D_2^+) complexes appears by far smaller than it is in the cases of the Li^+–H_2 (D_2) complexes. The consequences of omission of this component, like the undervaluation of the intensities $I_{[0\,0^0\,0]\to[0\,1^1\,0]}$ by ∼30 %, may be acceptable in studies of qualitative character.

Fig. F4. Temperature dependence of $I_{[v'']\to[v']}$

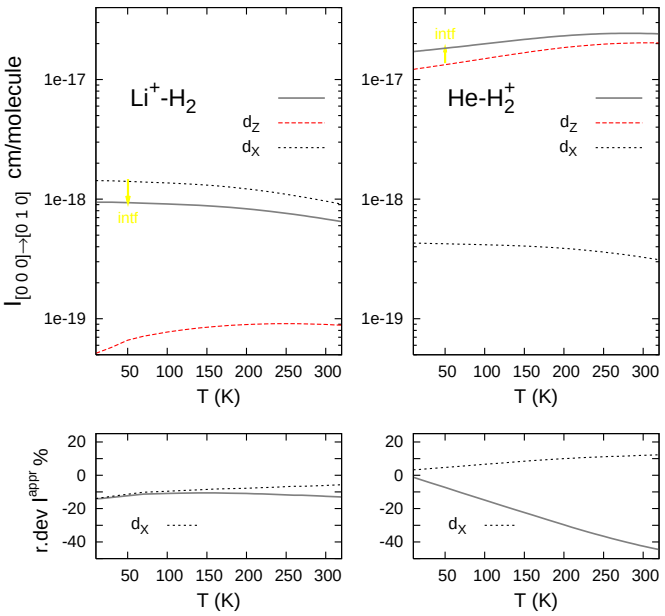

F4a. Functions $I_{[0\,0\,0]\to[0\,1\,0]}(T)$ of Li^+–H_2 and He–H_2^+

Each curve in the left panel represents the sum of 758 intensity functions $I_{i\to f}(T)$ of individual R-, P-, and Q-transitions in 7 subbands (K_a=3−2, ..., 3−4) of the band $[v_r\, v_\theta\, v_R]$=[0 0 0]→[0 1 0]. In the right panel, each curve is the sum of altogether 238 intensity functions of transitions in He–$p$$H_2$ and He–$o$$H_2$ in the subbands $[v_r\, v_b^k\, v_R]$=[0 0^0 0]→[0 1^1 0] and [0 1^1 0]→[0 2^2 0].

Full lines — the intensities account for the entire dipole vector **d**, broken lines — for the indicated component only.

The yellow arrows indicate the size and sign of d_Z−d_X interference contributions to the $I_{[0\,0\,0]\to[0\,1\,0]}$s.

In the bottom panels are errors of functions $I^{\rm appr}_{[0\,0\,0]\to[0\,1\,0]}(T)$ obtained with the approximate formula (C23) using the band strengths $S_{[0\,0\,0]\to[0\,1\,0]}$ and $S_{[0\,0\,0]\to[0\,1\,0]}(d_X)$.

To note is the qualitative difference between the broken black and read lines in the upper panels: the intensities induced by the components d_X decrease with T growing (the decrease is approximately described by formula (C23), as shown in the bottom panels) while the intensities induced by the components d_Z clearly increase with T, especially in the range up to ∼100 K. The difference is associated with the role of the λ-mixing. Namely, the dipole component d_X, connecting the components λ=$k_{\rm i}$ and λ=$k_{\rm f}$ of the initial ('i') and final ('f') states of transitions in the band, produces non-zero intensities no matter whether other λ-components do or do not exist in the states. The existence of the components $\lambda\neq k_{\rm i}$ and/or $\lambda\neq k_{\rm f}$ is indispensable, however, for the dipole component d_Z to become operating at all in these transitions. In ensembles of the complexes at a given temperature T, the populations of the components λ=k are likely to be close to the populations of the entire states, i.e. are determined by the energies of the states. The populations of the components $\lambda\neq k$ depend additionally on the Coriolis interactions. The additional strong dependence of these populations on the number J, hence, implicitly, on the rotational energies of the states, may be an explanation of the growth of the functions $I_{[0\,0\,0]\to[0\,1\,0]}(T)$ obtained from the calculations for both complexes in which the respective d_Z is the only component included and also from the calculations for He–H_2^+ with both components because the d_Z not d_X is decisive.

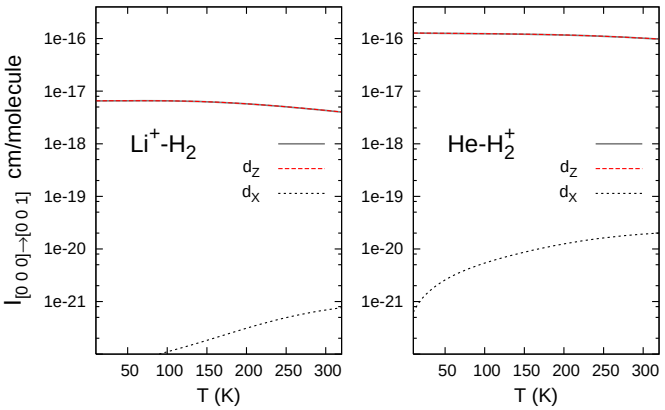

F4b. Functions $I_{[0\,0\,0]\to[0\,0\,1]}(T)$ of Li^+–H_2 and He–H_2^+

443 intensity functions $I_{i\to f}(T)$ of transitions in 4 subbands (K_a=0−0, ..., 3−3) of the band $[v_r\, v_\theta\, v_R]$=[0 0 0]→[0 0 1] are represented by each curve in the panel for Li^+–H_2.

Each of the respective curves in the panel for He–H_2^+ is formed of 205 functions $I_{i\to f}(T)$ that pertain to transitions in the subbands $[v_r\, v_b^k\, v_R]$=[0 0^0 0]→[0 0^0 1] and [0 1^1 1]→[0 1^1 1] of both He–$p$$H_2^+$ and He–$o$$H_2^+$.

Here, the intensities induced by the components d_Z of the dipole vectors of the complexes are the ones which decrease with growing temperature in a way well-describable by approximation (C23) (with deviations $|{\rm r.dev}I^{\rm appr}|$<5 %) and the intensities induced by the d_Xs behave quite differently. The explanation is analogous to that provided for the behaviour of the intensities $I_{[0\,0\,0]\to[0\,1\,0]}(T)$ induced by the d_Xs and the d_Zs, respectively.

TABLE FIII. He–$p\mathrm{H}_2^+$. Frequencies (ν, in cm^{-1}) and strengths (S, in a.u.) of several lowest $R(J^p)$, $P(J^p)$, and $Q(J^p)$ lines (for $J\leq 6$) in four $[v_r\, v_b^k\, v_R]\rightarrow[v_r'\, v_b^{'k'}\, v_R']$ bands in the far-infrared ($v_r=v_r'$). Results from the PES02 (Ref. 1) and the DMS97 (Ref. 2), generated in Refs. 1, 3, and 11 and in this work, compared to results from the newest electronic structure data PES19+DMS21 (Refs. 4 and 5), obtained in Ref. 5 using two different variational nuclear-motion approaches, termed CCVM and D^2FOPI — the results quoted in the second and third lines, respectively, below the lines with J values. E_i — the energy (in cm^{-1}) of the initial ro-vibrational state $[v_r\, v_b^k\, v_R]Jp$ relative to the dissociation threshold of the complex. δS — the relative percentage deviation of the present S value from the CCVM result.

		$R(J^p)$			$P(J^p)$			$Q(J^p)$		
J^p	E_i	ν	S	δS	ν	S	δS	ν	S	δS
					$[0\,0^0\,0]\rightarrow[0\,0^0\,0]$					
0	−1763.533	8.152	2.186[a]	0.0						
	−1793.910	8.164	2.186							
		8.165	1.999							
1	−1755.381	16.294	4.378	0.0						
	−1785.746	16.320	4.378							
		16.320	4.009							
2	−1739.087	24.419	6.583	0.0						
	−1769.426	24.457	6.582							
		24.458	6.021							
3	−1714.668	32.517	8.806	0.0						
	−1744.969	32.568	8.805							
		32.568	8.057							
4	−1682.151	40.577	11.055	0.0						
	−1712.401	40.642	11.053							
5	−1641.574	48.593	13.335							
	−1671.759	48.671	13.334	0.0						
					$[0\,1^1\,0]\rightarrow[0\,1^1\,0]$					
1^e	−1123.974	15.675	3.623	0.2				0.330	3.601	0.1
	−1153.892	15.731	3.616					0.321	3.596	
		15.731	3.354					0.321	3.333	
2^e	−1108.299	23.464	6.471	0.2				0.997	1.991	0.1
	−1138.161	23.550	6.458					0.969	1.990	
		23.551	5.984					0.970	1.840	
3^e	−1084.835	31.194	9.161	0.2				2.014	1.384	0.0
	−1114.611	31.312	9.141					1.957	1.383	
		31.313	8.487					1.958	1.280	
4^e	−1053.641	38.838	11.833	0.3				3.404	1.056	−0.1
	−1083.299	38.994	11.802					3.306	1.057	
								3.306	0.975	
5^e	−1014.803	46.373	14.549	0.3				5.203	0.847	−0.3
	−1044.305	46.571	14.502					5.044	0.849	
6^e	−968.430	53.761	17.354					7.455	0.700	−0.5
								7.217	0.702	
1^f	−1123.644	16.342	3.618	0.2						
	−1153.571	16.379	3.612							
		16.380	3.345							
2^f	−1107.302	24.481	6.453	−2.0						
	−1137.192	24.538	6.582							
		24.539	5.974							
3^f	−1082.821	32.584	9.116	0.2						
	−1112.654	32.660	9.100							
		32.661	8.431							
4^f	−1050.237	40.637	11.736	0.2						
	−1079.994	40.733	11.715							
5^f	−1009.600	48.625	14.365	0.2						
	−1039.260	48.743	14.339							

TABLE FIII. continued

					$[0\,0^0\,0] \rightarrow [0\,0^0\,1]$					
0	−1763.533	733.643	6.454 (−2)[b]	−2.4						
		738.964	6.610 (−2)							
		738.827	7.276 (−2)							
1	−1755.381	740.192	1.245 (−1)	−2.5	718.137	6.893 (−2)	−2.1			
		745.524	1.277 (−1)		723.433	7.039 (−2)				
		745.389	1.417 (−1)		723.296	7.687 (−2)				
2	−1739.087	745.934	1.794 (−1)	−2.8	709.197	1.421 (−1)	−2.1			
		751.275	1.845 (−1)		714.480	1.449 (−1)				
		751.141	2.058 (−1)		714.342	1.575 (−1)				
3	−1714.668	750.868	2.287 (−1)	−3.0	699.479	2.193 (−1)	−1.9			
		756.214	2.359 (−1)		704.748	2.235 (−1)				
		756.081	2.659 (−1)		704.611	2.427 (−1)				
4	−1682.151	755.001	2.717 (−1)	−3.4	688.998	3.005 (−1)	−1.8			
		760.345	2.812 (−1)		694.250	3.060 (−1)				
					694.114	3.312 (−1)				
5	−1641.574	758.349	3.073 (−1)	−3.4	677.774	3.854 (−1)	−1.7			
		763.679	3.195 (−1)		683.004	3.922 (−1)				
6	−1592.981	760.939	3.340 (−1)		665.831	4.733 (−1)	−1.7			
					671.032	4.816 (−1)				
					$[0\,0^0\,0] \rightarrow [0\,1^1\,0]$					
0	−1763.533	639.559	9.851 (−3)	3.1						
		640.018	9.552 (−3)							
		639.988	6.514 (−3)							
1	−1755.381	647.082	1.868 (−2)	3.6				631.737	1.132 (−2)	2.5
		647.584	1.803 (−2)					632.175	1.105 (−2)	
		647.554	1.304 (−2)					632.144	7.007 (−3)	
2	−1739.087	654.252	3.081 (−2)	4.0	615.113	1.878 (−3)	0.4	631.785	1.886 (−2)	2.5
		654.815	2.962 (−2)		615.534	1.870 (−3)		632.234	1.840 (−2)	
		654.785	2.243 (−2)		615.503	9.134 (−4)		632.204	1.167 (−2)	
3	−1714.668	661.027	4.693 (−2)	4.3	606.369	2.259 (−3)	−1.7	631.847	2.638 (−2)	2.5
		661.670	4.498 (−2)		606.807	2.300 (−3)		632.315	2.574 (−2)	
		661.640	3.553 (−2)		606.776	8.479 (−4)		632.285	1.637 (−2)	
4	−1682.151	667.348	6.797 (−2)	4.7	597.316	1.614 (−3)	−6.0	631.914	3.388 (−2)	2.5
		668.096	6.494 (−2)		597.790	1.718 (−3)		632.408	3.306 (−2)	
					597.758	3.171 (−4)		632.377	2.105 (−2)	
5	−1641.574	673.144	9.506 (−2)	4.9	587.933	5.635 (−4)	−18.0	631.974	4.135 (−2)	2.5
		674.025	9.060 (−2)		588.460	6.869 (−4)		632.499	4.035 (−2)	
6	−1592.981	678.312	1.297 (−1)		578.178	1.996 (−6)	−71.6	632.006	4.878 (−2)	2.5
					578.784	7.028 (−6)		632.571	4.761 (−2)	

[a] The purely vibrational line strength, i.e., using J=0 functions for both the initial and final state, is 2.192 $(ea_0)^2$ (14.16 D^2). The value obtained in Ref. 2 from the same DMS but an older PES[12], is 14.4 D^2.

[b] The purely vibrational counterpart, 6.769×10^{-2} (0.437 D^2), is identical to the value listed in Table 4 of Ref. 2.

TABLE FIV. Same as Table FIII for He–oD$_2^+$ except for the two facts: 1) two bands with v_r=0→1 excitation, in the near-infrared, are added, and 2) all results using the older electronic structure input (PES02+DMS97) have been calculated in this work.

		$R(J^p)$			$P(J^p)$			$Q(J^p)$		
J^p	E_i	ν	S	δS	ν	S	δS	ν	S	δS
					$[0\,0^0\,0] \rightarrow [0\,0^0\,0]$					
0	−1961.991	5.243	0.891	−0.3						
	−1995.022	5.249	0.894							
		5.251	0.836							
1	−1956.748	10.481	1.784	−0.3						
	−1989.773	10.496	1.789							
		10.499	1.677							
2	−1946.267	15.715	2.681	−0.3						
	−1979.277	15.735	2.688							
		15.740	2.517							
3	−1930.552	20.937	3.583	−0.3						
	−1963.542	20.965	3.593							
		20.973	3.370							
4	−1909.615	26.147	4.493	−0.3						
	−1942.577	26.182	4.505							
5	−1883.468	31.342	5.411	−0.3						
	−1916.394	31.383	5.426							
					$[0\,1^1\,0] \rightarrow [0\,1^1\,0]$					
1^e	−1483.290	10.293	1.461	−0.2				0.135	1.458	−0.2
	−1516.669	10.314	1.463					0.134	1.460	
		10.317	1.385					0.134	1.381	
2^e	−1472.997	15.429	2.603	−0.2				0.405	0.809	−0.2
	−1506.355	15.460	2.607					0.401	0.811	
		15.464	2.464					0.401	0.765	
3^e	−1457.568	20.550	3.673	−0.2				0.811	0.566	−0.2
	−1490.894	20.593	3.678					0.803	0.567	
		20.598	3.482					0.804	0.536	
4^e	−1437.018	25.654	4.721	−0.2				1.356	0.436	−0.2
	−1470.301	25.708	4.727					1.342	0.437	
								1.344	0.412	
5^e	−1411.364	30.734	5.766	−0.2				2.041	0.354	−0.2
	−1444.593	30.800	5.773					2.020	0.355	
6^e	−1380.630	35.787	6.817					2.869	0.298	−0.2
								2.838	0.299	
1^f	−1483.155	10.563	1.461	−0.2						
	−1516.535	10.582	1.463							
		10.584	1.382							
2^f	−1472.592	15.835	2.602	−3.2						
	−1505.954	15.735	2.688							
		15.867	2.466							
3^f	−1456.757	21.095	3.670	−0.2						
	−1490.091	21.132	3.675							
		21.138	3.474							
4^f	−1435.662	26.339	4.714	4.6						
	−1468.959	26.182	4.505							
5^f	−1409.323	31.562	5.755	−0.2						
	−1442.574	31.618	5.764							

TABLE FIV. continued

					$[0\,0^0\,0] \rightarrow [0\,0^0\,1]$					
0	−1961.991	641.808	3.856 (−2)	−3.2						
		645.800	3.983 (−2)							
		645.562	4.805 (−2)							
1	−1956.748	646.252	7.599 (−2)	−3.2	631.720	3.974 (−2)	−3.1			
		650.260	7.854 (−2)		635.694	4.099 (−2)				
		650.022	9.514 (−2)		635.454	4.927 (−2)				
2	−1946.267	650.291	1.123 (−1)	−3.3	626.084	8.068 (−2)	−3.0			
		654.319	1.161 (−1)		630.055	8.320 (−2)				
		654.078	1.410 (−1)		629.812	9.965 (−2)				
3	−1930.552	653.918	1.475 (−1)	−3.4	620.056	1.229 (−1)	−3.0			
		657.972	1.526 (−1)		624.029	1.267 (−1)				
		657.728	1.862 (−1)		623.783	1.516 (−1)				
4	−1909.615	657.130	1.816 (−1)	−3.4	613.639	1.664 (−1)	−2.9			
		661.213	1.880 (−1)		617.619	1.714 (−1)				
					617.365	2.047 (−1)				
5	−1883.468	659.910	2.145 (−1)	−3.5	606.834	2.112 (−1)	−2.9			
		664.035	2.222 (−1)		610.824	2.176 (−1)				
6	−1852.126	662.277	2.461 (−1)		599.641	2.575 (−1)	−2.8			
					603.647	2.652 (−1)				
					$[0\,0^0\,0] \rightarrow [0\,1^1\,0]$					
0	−1961.991	478.701	4.390 (−3)	3.3						
		478.353	4.252 (−3)							
		478.879	2.755 (−3)							
1	−1956.748	483.751	7.487 (−3)	3.2				473.593	5.738 (−3)	3.3
		483.418	7.256 (−3)					473.237	5.552 (−3)	
		483.945	4.921 (−3)					473.762	3.425 (−3)	
2	−1946.267	488.699	1.127 (−2)	3.1	462.977	1.399 (−3)	3.6	473.675	9.562 (−3)	3.3
		488.383	1.093 (−2)		462.608	1.351 (−3)		473.324	9.253 (−3)	
		488.910	7.691 (−3)		463.129	7.274 (−4)		473.847	5.704 (−3)	
3	−1930.552	493.534	1.580 (−2)	3.1	457.555	2.331 (−3)	3.7	473.795	1.338 (−2)	3.3
		493.241	1.533 (−2)		457.187	2.248 (−3)		473.451	1.295 (−2)	
		493.768	1.119 (−2)		457.706	1.106 (−3)		473.974	8.006 (−3)	
4	−1909.615	498.251	2.117 (−2)	3.0	452.047	2.844 (−3)	3.8	473.953	1.720 (−2)	3.3
		497.983	2.054 (−2)		451.682	2.741 (−3)		473.618	1.665 (−2)	
					452.197	1.192 (−3)		474.139	1.029 (−2)	
5	−1883.648	502.838	2.746 (−2)	3.0	446.450	2.988 (−3)	3.9	474.145	2.102 (−2)	3.3
		502.601	2.667 (−2)		446.093	2.876 (−3)		473.821	2.034 (−2)	
6	−1852.126	507.283	3.480 (−2)		440.762	2.818 (−3)	4.0	474.365	2.484 (−2)	3.3
					440.417	2.710 (−3)		474.056	2.404 (−2)	
					$[0\,0^0\,0] \rightarrow [1\,0^0\,0]$					
0	−1961.991	1321.478	9.469 (−3)	−5.1						
		1322.653	9.983 (−3)							
		1323.845	1.136 (−2)							
1	−1956.748	1326.487	1.866 (−2)	−5.4	1311.105	9.581 (−3)	−4.9			
		1327.670	1.973 (−2)		1312.268	1.008 (−2)				
		1328.864	2.245 (−2)		1313.457	1.140 (−2)				
2	−1946.267	1331.370	2.740 (−2)	−5.8	1305.754	1.910 (−2)	−5.0			
		1332.563	2.909 (−2)		1306.908	2.010 (−2)				
		1333.757	3.320 (−2)		1308.095	2.273 (−2)				
3	−1930.552	1336.109	3.556 (−2)	−6.3	1300.291	2.838 (−2)	−5.2			
		1337.322	3.795 (−2)		1301.440	2.992 (−2)				
		1338.516	4.330 (−2)		1302.625	3.370 (−2)				
4	−1909.615	1340.690	4.296 (−2)	−6.9	1294.718	3.726 (−2)	−5.4			
		1341.937	4.616 (−2)		1295.862	3.941 (−2)				
					1297.044	4.434 (−2)				
5	−1883.468	1345.090	4.945 (−2)	−7.7	1289.025	4.558 (−2)	−5.9			
		1346.393	5.358 (−2)		1290.175	4.841 (−2)				
6	−1852.126	1349.274	5.478 (−2)		1283.201	5.316 (−2)	−6.4			
					1284.372	5.679 (−2)				

TABLE FIV. continued

					$[0\,0^0\,0] \rightarrow [1\,1^1\,0]$					
0	−1961.991	1825.679	4.530 (−5)	39.4						
		1825.301	3.250 (−5)							
		1826.596	2.009 (−5)							
1	−1956.748	1830.971	5.894 (−5)	30.7				1820.490	7.135 (−5)	38.5
		1830.022	4.509 (−5)					1820.094	5.151 (−5)	
		1831.244	3.688 (−5)					1821.387	2.253 (−5)	
2	−1946.267	1835.709	7.715 (−5)	60.5	1809.046	2.580 (−5)	37.4	1820.671	1.080 (−4)	29.3
		1833.904	4.808 (−5)		1809.556	1.877 (−5)		1819.657	8.357 (−5)	
		1834.782	5.125 (−5)		1810.846	3.472 (−6)		1820.870	3.614 (−5)	
3	−1930.552	1840.026	7.523 (−5)	46.9	1804.775	4.770 (−5)	27.0	1820.368	1.519 (−4)	56.3
		1841.876	5.121 (−5)		1803.791	3.754 (−5)		1818.376	9.720 (−5)	
		1842.771	4.265 (−5)		1805.005	3.925 (−6)		1819.209	3.752 (−5)	
4	−1909.615	1843.749	9.307 (−5)	2.3	1799.057	5.072 (−5)	3.5	1819.702	1.937 (−4)	89.9
		1845.245	9.102 (−5)		1797.203	4.902 (−5)		1821.385	1.020 (−4)	
					1798.069	1.202 (−6)		1822.293	4.821 (−5)	
5	−1883.468	1846.202	9.699 (−5)	62.1	1792.942	8.104 (−5)	81.8	1818.481	2.278 (−4)	43.6
		1848.798	5.983 (−5)		1794.728	4.457 (−5)		1819.959	1.586 (−4)	
6	−1852.126	1851.009	5.734 (−5)		1786.260	1.257 (−4)	99.8	1815.921	2.309 (−4)	20.5
					1787.679	6.291 (−5)		1818.571	1.916 (−4)	

COMMENTS

(i). As shown in Tables FIII and FIV, the strengths obtained from the PES02+DMS97 agree with the strengths generated from the PES19+DMS21 with the CCVM method

- excellently – for the lines in the pure rotational bands ($|\delta S|$<1 % for most lines shown),
- very good – for the lines in the fundamental atom-diatom bending and stretching bands ($|\delta S|$<5 % for 55 of the total of 58 such lines shown in the spectra of both complexes),
- fairly good – for the lines in the fundamental diatomic stretching band in the spectrum of He–D_2^+ (the deviations δS between −5 and −8 %).

Understandably, the agreement may be much worse if the strengths concern weak transitions to highly excited states (the mode mixing is more likely in these states, the mixing is sensitive to properties of the PES on which the states lie, and the PES02 differs from the PES19 most significantly just in the upper part of the well and the bottom part of the He+H_2^+ fragmentation valley). An example here is the comparison of the line strengths in the band $[0\,0^0\,0]\rightarrow[1\,1^1\,0]$ of He–D_2^+ (the upper state energies lie from 136 to 1 cm^{-1} below the dissociation limit): the deviations δS vary from 2 to 100 %, the average size – 45 %.

(ii) The very good agreement of the 'PES02+DMS97' and the 'PES19+DMS21(CCVM)' results stated here for the line strengths in the fundamental bands of both types, the *b*-type (perpendicular) atom-diatom bending and the *a*-type (parallel) stretching bands, testifies on: (a) the comparable accuracy of the DMS97 and DMS21 data for the dipole moment components d_Z and d_X, (b) the consistency of the procedures used in both calculations to account for both these components. Obviously, the procedures used in calculations of the 'PES02+DMS97' results were the same as used in the calculations of the spectra of Li^+–H_2 (D_2). Thus, conclusion (b) of the present comparison may be counted as a realization of goal (1) of this material (see page 6).

(iii) Rather unexpected fact emerges from Tables FIII and FIV concerning the comparison of the strengths calculated with the two nuclear-dynamics methods (D^2FOPI and CCVM) from the same electronic structure input (PES19+DMS21): in nearly all cases these strengths are evidently less consistent than the strengths from the two different input data, PES02+DMS97 and PES19+DMS21, obtained with the present close-coupling (CC) method and the CCVM, respectively. One of the likely causes is indicated in Table FVII.

Vibrational spectra of $\mathbf{He}$–$\mathbf{H}_2^+$ and $\mathbf{He}$–$\mathbf{D}_2^+$ from different electronic structure data

TABLE FV. Vibrational band origins, $\left[E([v_r\, v_b^k\, v_R], J^p{=}k^e) - E([0\,0^0\,0], J{=}0)\right]/hc$, in the spectra of the He–H_2^+ and He–D_2^+ complexes. Results from several PESs, including the PES02 — a supplement to the comparison presented in Table 3 of Ref. 5.

He–H_2^+	PES19[a]		PES12[b]		PES02[c]		PES99[d]		PES97[e]		PES95[f]	
$[v_r\, v_b^k\, v_R]$	j odd	j even	j odd	j even	j odd	j even	j odd	j even	j odd	j even	j odd	j even
$[0\,1^1\,0]$	640.0	640.0	647.5	647.5	639.5[g]	639.5[g]	646.1	646.2	643.1	643.0	643.0	643.1
$[0\,0^0\,1]$	731.6	731.6	733.7	733.7	726.3[g]	726.3[g]	715.9	715.9	717.7	717.6	717.8	717.7
$[0\,2^0\,0]$	1136.1	1134.1	1151.8	1150.1	1133.2[g]	1131.1[g]			1137.6	1135.6	1137.6	1135.4
$[0\,0^0\,2]$	1256.4	1255.6	1264.2	1263.6	1246.1[g]	1245.4[g]			1231.1	1230.3	1230.9	1230.3
$[0\,2^0\,2]$	1604[h]		1621[h]		1590.8[g]							
$[1\,0^0\,0]$	1812.3		1809.0	1822.6[l]	1795.1[g,i]	1823.0[j]	1825[m]	1825[m]	1836.1[n]	1836.1[n]	1843.8[n]	1843.8[n]
	1833.5		1832.0		1816.4[g,i]							
					1850.0[k]							
He–D_2^+												
$[0\,1^1\,0]$	478.4	478.4			478.7[o]	478.7[o]					481.0	481.2
$[0\,0^0\,1]$	640.9	640.9			637.0	637.0					629.5	629.5
$[0\,2^0\,0]$	891.1	891.1			891.4	891.4					896.5	896.5
$[0\,0^0\,2]$	1139.6	1139.6			1130.9	1130.9					1116.8	1116.7
$[1\,0^0\,0]$	1317.6	1317.5			1316.4	1316.3					1326.2[n]	1326.1[n]
$[0\,2^0\,1]$	1376.0[p]	1375.6[p]			1371.1	1370.7						
$[0\,0^0\,3]$	1511.6[p]	1511.5[p]			1497.7	1497.6						

[a] Ref. 4 and Ref. 5. [b] Ref. 13 and Ref. 14. [c] Ref. 1 and Refs. 3 and 7. [d] Ref. 15. [e] Refs. 2 and 9. [f] Ref. 12.

[g] Results from Table II of Ref. 3. They are nearly identical to some of the results published together with the PES02, in Tables 2 and 3 of Ref. 1.

[h] Unassigned in Ref. 5. The assignment listed here concerns the energy from the PES02.

[i] These energies were actually not assigned to the state $[1\,0^0\,0]$ in Ref. 3. The NEA of the respective functions, performed here in somewhat extended way, revealed that they do contain orbital $[1\,0^0\,0]$ but occupied in 10 and 20% only. See Fig. F6a.

[j] Result from Table AI of Ref. 7; pertains to resonance of width Γ=8.2 cm^{-1} determined in the life-time matrix calculations.

[k] Determined here — a resonance of width Γ=2.4 cm^{-1}. Listed in Tables AIV and AV of Ref. 7 are energies and widths of the subsequent J=1 and J=2 resonances.

[l] From Table 3 of Ref. 14 — a resonance of width Γ=0.12 cm^{-1} determined from the PES12 with a complex-scaling method. Though incomparably sharper, this resonance has energy relative to the ground state quite close to the energy obtained from the PES02 (footnote j).

[m] Resonance energy determined approximately. Note that the subsequent accurate resonance calculations using the PES02 and the PES12 gave very close values for the complex with pH$_2^+$ (footnotes j and l.)

[n] Determined approximately using an adiabatic separation scheme.

[o] All numbers in the column are results of this work.

[p] Unassigned in Ref. 5. In the first column, there are assignments proposed in this work, based on the NEA of the respective functions from the PES02 (Table FI, Fig. F6b) and the comparisons of the absorption cross-sections and intensities presented in Fig. F5 and Table FVII.

Fig. F5. Absorption cross-section at T=15 K

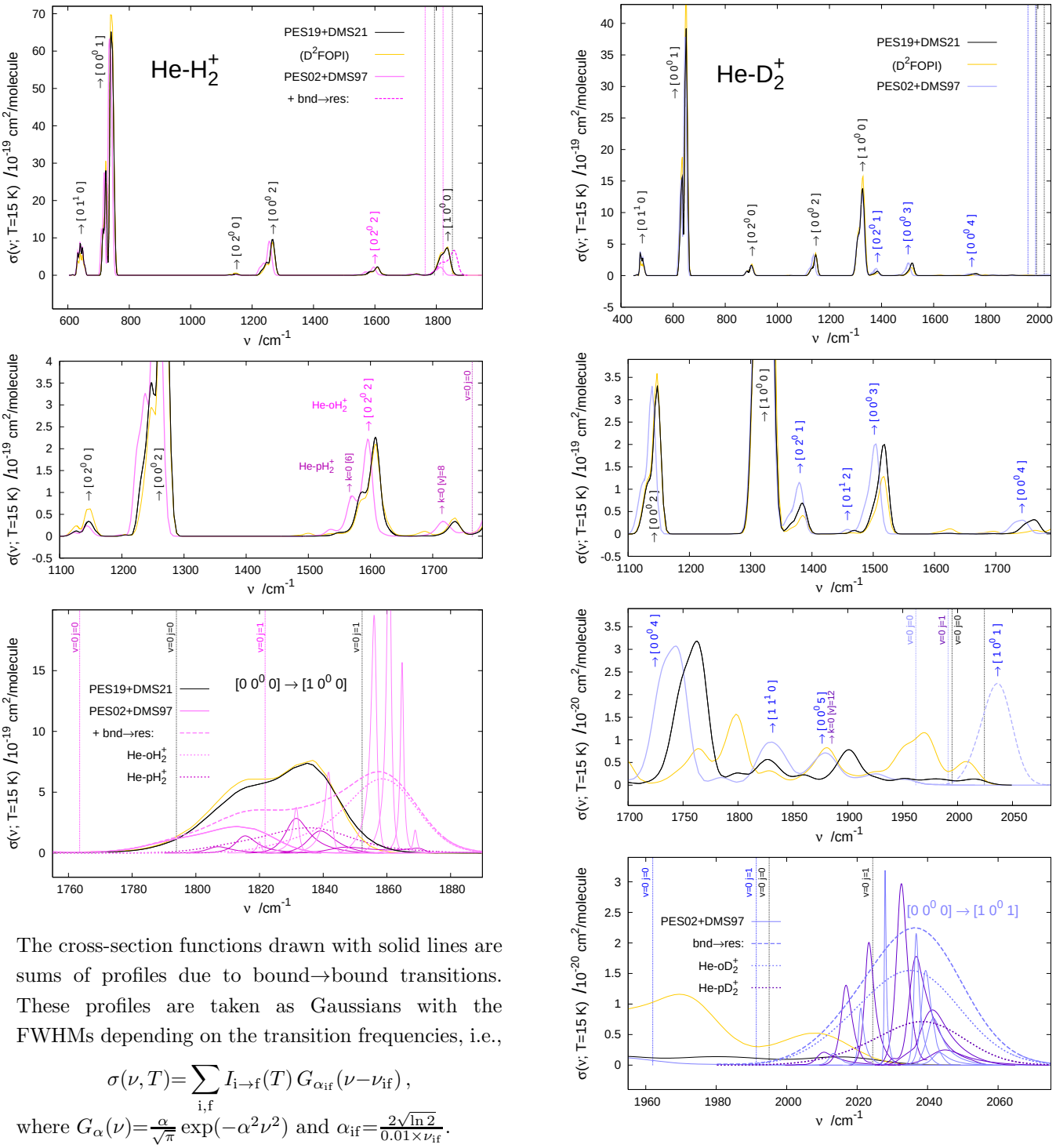

The cross-section functions drawn with solid lines are sums of profiles due to bound→bound transitions. These profiles are taken as Gaussians with the FWHMs depending on the transition frequencies, i.e.,

$$\sigma(\nu,T)=\sum_{\mathrm{i,f}} I_{\mathrm{i}\to\mathrm{f}}(T)\, G_{\alpha_{\mathrm{if}}}(\nu-\nu_{\mathrm{if}})\,,$$

where $G_\alpha(\nu)=\frac{\alpha}{\sqrt{\pi}}\exp(-\alpha^2\nu^2)$ and $\alpha_{\mathrm{if}}=\frac{2\sqrt{\ln 2}}{0.01\times\nu_{\mathrm{if}}}$.

The intensities $I_{\mathrm{i}\to\mathrm{f}}(15\,\mathrm{K})$ and the frequencies ν_{if} of all transitions included are listed in Tables FVI and FVII.

The bound→resonance contributions, drawn with dashed lines, are obtained as $\sum_{\mathrm{i,f}}(G_{\alpha_{\mathrm{if}}}\star\sigma_{\mathrm{i}\to\mathrm{f}^{\mathrm{res}}})(\nu;T)$, where $\sigma_{\mathrm{i}\to\mathrm{f}^{\mathrm{res}}}(\nu;T)$ denotes a resonance profile extracted from the bound→free ($E_{\mathrm{i}}^{\mathrm{B}}\to E$) absorption-cross section, $\sigma_{\mathrm{i}\to\mathrm{free}}(\nu;T)=\frac{2\pi^2}{3hc\varepsilon_0}\,\nu\,\frac{dS}{d\nu}(\nu)\,P_{\mathrm{i}}(T)[1-\exp(-hc\nu/k_BT)]$, with $\nu=\frac{E-E_{\mathrm{i}}^{\mathrm{B}}}{hc}$, the frequency differential strength $\frac{dS}{d\nu}$ defined by the rhs of Eq. 6, and the initial state population P_{i} – by Eq. 7 of the paper. The width parameter of the Gaussian, α_{if}, is defined as for bound→bound transitions taking $\nu_{\mathrm{if}}=\frac{E_{\mathrm{f}}^{\mathrm{res}}-E_{\mathrm{i}}^{\mathrm{B}}}{hc}$ and $E_{\mathrm{f}}^{\mathrm{res}}$ as the position of maximum in the profile $\sigma_{\mathrm{i}\to\mathrm{f}^{\mathrm{res}}}(\nu;T)$. The profiles $\sigma_{\mathrm{i}\to\mathrm{f}^{\mathrm{res}}}(\nu;T=15\,\mathrm{K})$ generated from the PES02+DMS97 to simulate the band $[0\,0^0\,0]\to[1\,0^0\,0]$ in the spectrum of He–H_2^+ and the band $[0\,0^0\,0]\to[1\,0^0\,1]$ in the spectrum of He–D_2^+ are shown in the bottom left and right panel, respectively.

TABLE FVI. Rotational lines in the vibrational subbands $[0\,0^0\,0]\rightarrow k\,[\mathrm{v}]$ of He–oH$_2^+$ and He–pH$_2^+$ forming the peaks observed in the plots of the absorption spectra in Fig. F5. Frequencies (ν, in cm^{-1}) and absolute intensities (I, in cm/molecule) of the lines. Comparison of results from the two different electronic structure data (PES02+DMS97 and PES19+DMS21) and the three different nuclear motion approaches (CC, CCVM, and D^{2}FOPI) in terms of absolute deviations $\Delta\nu$ and relative percentage deviations δI. Complete assignment of the subbands $k\,[\mathrm{v}]$, with the numbers $[v_r\, v_b^k\, v_R]$, confirmed or suggested by the NEA of the CC results from the PES02, see Fig. F6.

				PES02+DMS97		PES02+DMS97 vs PES19+DMS21		PES19+DMS21 CCVM		PES19+DMS21 D^{2}FOPI vs CCVM	
o/p	k	[v]	line	$[v_r\, v_b^k\, v_R]$				$[v_r\, v_b^k\, v_R]$			
				ν	I	$\Delta\nu$	δI	ν	I^a	$\Delta\nu$	δI^a
o	1	1		$[0\,1^1\,0]$				$[0\,1^1\,0]$			
			P(2)	615.08	7.667 (−20)	−0.42	0.6	615.500	7.621 (−20)	−0.030	−51.0
			Q(1)	631.70	2.261 (−18)	−0.44	2.4	632.137	2.207 (−18)	−0.030	−36.6
			Q(2)	631.75	7.890 (−19)	−0.45	2.7	632.199	7.684 (−19)	−0.031	−36.5
			R(0)	639.52	4.348 (−18)	−0.46	2.9	639.984	4.225 (−18)	−0.029	−31.7
			R(1)	647.06	3.814 (−18)	−0.51	3.5	647.560	3.685 (−18)	−0.030	−27.8
			R(2)	654.24	1.332 (−18)	−0.56	4.2	654.803	1.279 (−18)	−0.030	−24.2
p	1	1		$[0\,1^1\,0]$				$[0\,1^1\,0]$			
			P(2)	615.11	2.549 (−20)	−0.42	0.6	615.534	2.534 (−20)	−0.031	−51.2
			Q(1)	631.74	7.536 (−19)	−0.44	2.4	632.175	7.357 (−19)	−0.031	−36.6
			Q(2)	631.79	2.630 (−19)	−0.45	2.7	632.234	2.562 (−19)	−0.030	−36.6
			R(0)	639.56	1.450 (−18)	−0.46	2.9	640.018	1.409 (−18)	−0.030	−31.8
			R(1)	647.08	1.273 (−18)	−0.50	3.5	647.584	1.230 (−18)	−0.030	−27.7
			R(2)	654.25	4.448 (−19)	−0.56	4.2	654.815	4.271 (−19)	−0.030	−24.3
o	0	2		$[0\,0^0\,1]$				$[0\,0^0\,1]$			
			P(2)	709.23	6.672 (−18)	−5.28	−2.5	714.512	6.840 (−18)	−0.138	8.8
			P(1)	718.17	1.564 (−17)	−5.29	−2.8	723.468	1.609 (−17)	−0.138	9.0
			R(0)	733.68	3.271 (−17)	−5.32	−3.2	738.996	3.379 (−17)	−0.137	10.2
			R(1)	740.22	2.912 (−17)	−5.33	−3.3	745.552	3.010 (−17)	−0.137	10.7
			R(2)	745.96	8.862 (−18)	−5.34	−3.2	751.295	9.158 (−18)	−0.134	11.7
p	0	2		$[0\,0^0\,1]$				$[0\,0^0\,1]$			
			P(2)	709.20	2.224 (−18)	−5.28	−2.5	714.480	2.280 (−18)	−0.138	8.7
			P(1)	718.14	5.214 (−18)	−5.30	−2.8	723.433	5.364 (−18)	−0.137	9.2
			R(0)	733.64	1.090 (−17)	−5.32	−3.2	738.964	1.126 (−17)	−0.137	10.0
			R(1)	740.19	9.703 (−18)	−5.33	−3.3	745.524	1.003 (−17)	−0.135	10.9
			R(2)	745.93	2.953 (−18)	−5.34	−3.2	751.275	3.052 (−18)	−0.134	11.5
o	0	3		$[0\,2^0\,0]$				$[0\,2^0\,0]$			
			P(2)	1116.37	2.698 (−20)	−2.87	−30.3	1119.235	3.870 (−20)	−0.036	102.0
			P(1)	1125.04	7.201 (−20)	−2.85	−28.8	1127.889	1.011 (−19)	−0.037	98.3
			R(0)	1140.81	1.586 (−19)	−2.91	−28.8	1143.719	2.228 (−19)	−0.035	92.4
			R(1)	1147.88	1.306 (−19)	−2.98	−30.4	1150.862	1.877 (−19)	−0.036	94.7
			R(2)	1154.34	3.349 (−20)	−3.09	−33.7	1157.436	5.049 (−20)	−0.037	95.9
p	0	3		$[0\,2^0\,0]$				$[0\,2^0\,0]$			
			P(2)	1114.43	8.186 (−21)	−2.96	−31.5	1117.387	1.195 (−20)	−0.039	106.5
			P(1)	1122.97	2.192 (−20)	−2.95	−29.9	1125.914	3.127 (−20)	−0.039	99.5
			R(0)	1138.87	4.775 (−20)	−3.00	−30.2	1141.871	6.844 (−20)	−0.038	98.5
			R(1)	1146.19	3.862 (−20)	−3.07	−32.3	1149.259	5.706 (−20)	−0.038	98.8
			R(2)	1153.01	9.585 (−21)	−3.17	−36.4	1156.183	1.507 (−20)	−0.038	106.4
o	0	4		$[0\,0^0\,2]$				$[0\,0^0\,2]$			
			P(2)	1228.82	1.109 (−18)	−10.11	−3.4	1238.929	1.147 (−18)	−0.185	−14.9
			P(1)	1237.99	2.717 (−18)	−10.20	−3.4	1248.191	2.813 (−18)	−0.186	−14.3
			R(0)	1253.26	5.687 (−18)	−10.15	−4.4	1263.413	5.951 (−18)	−0.184	−10.6
			R(1)	1259.52	4.738 (−18)	−9.94	−6.6	1269.466	5.074 (−18)	−0.181	−8.6
			R(2)	1265.32	1.209 (−18)	−9.43	−13.1	1274.749	1.391 (−18)	−0.175	−4.9

TABLE FVI. continued

p	0	4			$[0\,0^0\,2]$				$[0\,0^0\,2]$		
			P(2)	1228.28	3.651 (−19)	−10.11	−3.6	1238.399	3.788 (−19)	−0.184	−15.4
			P(1)	1237.25	9.043 (−19)	−10.23	−3.5	1247.473	9.366 (−19)	−0.185	−13.7
			R(0)	1252.73	1.866 (−18)	−10.15	−4.8	1262.883	1.960 (−18)	−0.183	−10.5
			R(1)	1259.30	1.534 (−18)	−9.93	−7.0	1269.227	1.650 (−18)	−0.180	−7.5
			R(2)	1265.28	3.958 (−19)	−9.46	−12.3	1274.748	4.515 (−19)	−0.175	−4.9
o	0	6			$[0\,2^0\,2]$				$[0\,2^0\,2]^b$		
			P(2)	1570.87	3.026 (−19)	−12.47	1.4	1583.337	2.983 (−19)	−0.162	1.2
			P(1)	1582.71	7.980 (−19)	−13.09	−4.9	1595.801	8.394 (−19)	−0.174	−2.8
			R(0)	1595.32	1.713 (−18)	−12.50	0.0	1607.821	1.713 (−18)	−0.161	−9.0
			R(2)	1596.29	4.471 (−19)	−11.67	−1.7	1607.959	4.549 (−19)	−0.153	−4.2
			R(1)	1596.95	1.492 (−18)	−11.99	0.3	1608.938	1.488 (−18)	−0.155	−8.0
p	0	6			$[0\,0^0\,3]$				$[0\,0^0\,3]^b$		
			P(2)	1544.26	9.189 (−20)	−15.47	−3.0	1559.729	9.473 (−20)	−0.194	−22.2
			P(1)	1556.17	2.253 (−19)	−15.56	−2.7	1571.732	2.315 (−19)	−0.195	−24.7
			R(2)	1566.86	1.413 (−19)	−15.10	−2.7	1581.963	1.452 (−19)	−0.184	−23.2
			R(0)	1568.71	5.014 (−19)	−15.51	−1.7	1584.213	5.102 (−19)	−0.193	−26.5
			R(1)	1569.47	4.564 (−19)	−15.41	16.6	1584.878	3.913 (−19)	−0.196	−21.6
p	0	8			$[0\,0^0\,3]$				$[0\,0^0\,3]^b$		
			P(2)	1691.67	4.093 (−20)	−20.62	−14.8	1712.282	4.804 (−20)	−0.196	25.2
			P(1)	1704.27	1.020 (−19)	−20.68	−13.2	1724.948	1.174 (−19)	−0.197	23.0
			R(2)	1709.96	4.494 (−20)	−20.68	−27.4	1730.634	6.186 (−20)	−0.189	44.1
			R(1)	1715.33	1.797 (−19)	−20.61	−19.7	1735.939	2.238 (−19)	−0.194	32.7
			R(0)	1716.11	2.165 (−19)	−20.65	−15.5	1736.766	2.561 (−19)	−0.195	26.2
o	0	8			$[0\,0^0\,5]$				$[1\,0^0\,0]$		
			P(2)	1772.22	9.767 (−20)			1791.770	7.960 (−19)	0.175	18.5
			R(2)	1782.93	5.539 (−21)			1805.939	9.930 (−20)	0.074	65.2
			P(1)	1786.95	5.841 (−19)			1804.155	2.822 (−18)	0.307	13.8
			R(1)	1792.67	1.757 (−19)			1814.453	1.523 (−18)	0.032	27.5
			R(0)	1796.67	5.644 (−19)			1816.253	4.262 (−18)	0.177	15.7
o	0	9			$[0\,0^0\,6]$				$[1\,0^0\,0]$		
			P(2)	1794.02	4.327 (−19)			1812.347	1.267 (−18)	0.917	8.2
			P(1)	1808.23	1.962 (−18)			1825.308	3.084 (−18)	0.681	1.3
			R(1)	1812.73	3.731 (−19)			1834.945	4.447 (−18)	1.777	36.6
			R(0)	1818.47	2.320 (−18)			1836.831	6.722 (−18)	0.918	7.7
o	0	10			$[1\,0^0\,0]$				?		
			P(3)	1820.0	1.98 (−19)[c]			1803.223	2.266 (−21)		
			P(2)	1831.5	1.12 (−18)			1826.333	1.474 (−19)		
			P(1)	1841.7	2.26 (−18)			1841.400	6.414 (−19)		
			R(0)	1856.0	5.81 (−18)			1850.817	7.874 (−19)		
			R(1)	1860.7	6.58 (−18)			1844.000	8.091 (−20)		
			R(2)	1864.8	2.67 (−18)						
			R(3)	1868.9	3.44 (−19)						
p	0	11			$[1\,0^0\,0]$						
			P(2)	1807.1	5.49 (−19)[c]						
			P(1)	1815.6	1.38 (−18)						
			R(0)	1831.5	3.07 (−18)						
			R(1)	1839.2	2.07 (−18)						
			R(2)	1847.3	1.17 (−18)						

[a] The intensities evaluated according to Eq. (5) of the paper using the energies and the line strengths provided in Ref. 5 (partly quoted in Table FIII).

[b] The assignments suggested by the present NEA. They are supported by the outcome of the comparison 'PES02+DMS97 vs PES19+DMS21': small or uniform shifts $\Delta\nu$ of lines in the considered band and small or reasonable deviations δI. It is to note that the absolute values of the latter deviations are smaller (in some cases even above 10 times) than the absolute values of the δIs displayed by the comparison 'D^{2}FOPI vs CCVM'.

[c] The intensities in the column are integrals over the profiles $\sigma_{\mathrm{i}\to\mathrm{f}^{\mathrm{res}}}(\nu; T{=}15\,\mathrm{K})$ shown in Fig. F5.

TABLE FVII. Same as Table FVI for He–D_2^+ plus information on intensities obtained using the PES02+DMS97 without the d_X dipole component: the relative percentage deviations from the PES19+DMS21(CCVM) results listed within the slashes.

				PES02+DMS97		PES02+DMS97 vs PES19+DMS21		PES19+DMS21 CCVM		PES19+DMS21 D^2FOPI vs CCVM	
o/p	k	[v]	line	$[v_r\ v_b^k\ v_R]$				$[v_r\ v_b^k\ v_R]$			
				ν	I	$\Delta\nu$	$\delta I\ /\delta I(d_X{=}0)/^\natural$	ν	I^a	$\Delta\nu$	δI^a
o	1	1		$[0\,1^1\,0]$				$[0\,1^1\,0]$			
			P(3)	457.55	2.165 (−20)	0.37	4.0 / − 43.3/	457.187	2.081 (−20)	0.519	−50.8
			P(2)	462.98	5.935 (−20)	0.37	3.7 / − 40.0/	462.608	5.721 (−20)	0.521	−46.1
			Q(1)	473.59	6.806 (−19)	0.36	3.4 / − 34.7/	473.237	6.584 (−19)	0.525	−38.2
			Q(2)	473.67	4.151 (−19)	0.35	3.5 / − 34.6/	473.324	4.010 (−19)	0.523	−38.3
			Q(3)	473.79	1.287 (−19)	0.34	3.7 / − 34.4/	473.451	1.241 (−19)	0.523	−38.2
			R(0)	478.70	8.702 (−19)	0.35	3.2 / − 32.6/	478.353	8.431 (−19)	0.526	−35.1
			R(1)	483.75	9.072 (−19)	0.33	3.2 / − 30.5/	483.418	8.790 (−19)	0.527	−32.1
			R(2)	488.70	5.046 (−19)	0.32	3.3 / − 28.6/	488.383	4.886 (−19)	0.527	−29.6
			R(3)	493.53	1.583 (−19)	0.29	3.4 / − 26.9/	493.241	1.530 (−19)	0.527	−27.0
p	1	1		$[0\,1^1\,0]$				$[0\,1^1\,0]$			
			P(3)	457.55	1.083 (−20)	0.37	4.1 / − 43.3/	457.187	1.040 (−20)	0.518	−50.9
			P(2)	462.98	2.968 (−20)	0.37	3.8 / − 40.0/	462.608	2.861 (−20)	0.521	−46.0
			Q(1)	473.59	3.404 (−19)	0.35	3.4 / − 34.7/	473.237	3.292 (−19)	0.524	−38.3
			Q(2)	473.67	2.076 (−19)	0.35	3.5 / − 34.5/	473.323	2.005 (−19)	0.524	−38.2
			Q(3)	473.79	6.438 (−20)	0.34	3.7 / − 34.4/	473.451	6.206 (−20)	0.522	−38.3
			R(0)	478.70	4.352 (−19)	0.35	3.2 / − 32.5/	478.353	4.216 (−19)	0.526	−35.0
			R(1)	483.75	4.537 (−19)	0.33	3.2 / − 30.5/	483.418	4.395 (−19)	0.527	−32.2
			R(2)	488.70	2.524 (−19)	0.31	3.3 / − 28.6/	488.383	2.443 (−19)	0.527	−29.5
			R(3)	493.53	7.916 (−20)	0.29	3.4 / − 26.8/	493.241	7.652 (−20)	0.526	−27.1
o	0	2		$[0\,0^0\,1]$				$[0\,0^0\,1]$			
			P(3)	620.06	1.547 (−18)	−3.97	−3.3 / − 3.8/	624.029	1.600 (−18)	−0.246	19.6
			P(2)	626.08	4.629 (−18)	−3.97	−3.6 / − 3.9/	630.055	4.800 (−18)	−0.243	19.7
			P(1)	631.72	6.286 (−18)	−3.97	−3.7 / − 4.0/	635.694	6.530 (−18)	−0.240	20.1
			R(0)	641.81	1.025 (−17)	−3.99	−3.9 / − 3.9/	645.800	1.066 (−17)	−0.238	20.6
			R(1)	646.25	1.230 (−17)	−4.01	−3.9 / − 3.8/	650.260	1.280 (−17)	−0.238	21.1
			R(2)	650.29	6.693 (−18)	−4.03	−3.8 / − 3.6/	654.319	6.958 (−18)	−0.241	21.3
			R(3)	653.92	1.958 (−18)	−4.05	−3.7 / − 3.3/	657.972	2.033 (−18)	−0.244	21.8
p	0	2		$[0\,0^0\,1]$				$[0\,0^0\,1]$			
			P(3)	620.06	7.735 (−19)	−3.97	−3.3 / − 3.8/	624.029	7.999 (−19)	−0.248	19.4
			P(2)	626.09	2.315 (−18)	−3.97	−3.5 / − 3.9/	630.055	2.400 (−18)	−0.242	19.8
			P(1)	631.72	3.144 (−18)	−3.97	−3.7 / − 4.0/	635.694	3.265 (−18)	−0.240	20.0
			R(0)	641.81	5.126 (−18)	−3.99	−3.9 / − 3.9/	645.800	5.332 (−18)	−0.237	20.7
			R(1)	646.25	6.151 (−18)	−4.01	−3.9 / − 3.8/	650.260	6.398 (−18)	−0.239	20.9
			R(2)	650.29	3.347 (−18)	−4.03	−3.8 / − 3.6/	654.319	3.479 (−18)	−0.241	21.4
			R(3)	653.92	9.792 (−19)	−4.05	−3.7 / − 3.3/	657.972	1.016 (−18)	−0.245	21.7
o	0	3		$[0\,2^0\,0]$				$[0\,2^0\,0]$			
			P(3)	875.44	7.408 (−20)	0.34	−5.5 / − 2.7/	875.101	7.838 (−20)	1.694	12.2
			P(2)	880.85	2.264 (−19)	0.35	−5.6 / − 3.2/	880.508	2.398 (−19)	1.699	12.5
			P(1)	886.18	3.127 (−19)	0.34	−5.7 / − 3.6/	885.835	3.316 (−19)	1.704	12.0
			R(0)	896.58	5.221 (−19)	0.32	−5.6 / − 4.1/	896.253	5.532 (−19)	1.704	11.7
			R(1)	901.64	6.308 (−19)	0.31	−5.5 / − 4.3/	901.331	6.675 (−19)	1.703	10.7
			R(2)	906.59	3.445 (−19)	0.28	−5.3 / − 4.4/	906.308	3.638 (−19)	1.699	10.2
			R(3)	911.42	1.008 (−19)	0.25	−5.1 / − 4.6/	911.167	1.062 (−19)	1.693	8.9
p	0	3		$[0\,2^0\,0]$				$[0\,2^0\,0]$			
			P(3)	875.44	3.705 (−20)	0.33	−5.5 / − 2.7/	875.102	3.919 (−20)	1.694	12.5
			P(2)	880.85	1.132 (−19)	0.34	−5.6 / − 3.2/	880.510	1.199 (−19)	1.700	12.2
			P(1)	886.18	1.564 (−19)	0.34	−5.6 / − 3.5/	885.838	1.658 (−19)	1.704	12.4
			R(0)	896.57	2.612 (−19)	0.32	−5.6 / − 4.1/	896.255	2.766 (−19)	1.705	11.3
			R(1)	901.63	3.155 (−19)	0.30	−5.5 / − 4.3/	901.333	3.338 (−19)	1.703	11.0

TABLE FVII. continued

			R(2)	906.58	1.723 (−19)	0.27	−5.3	/ − 4.4/	906.309	1.819 (−19)	1.699	9.9
			R(3)	911.41	5.042 (−20)	0.24	−5.0	/ − 4.5/	911.166	5.310 (−20)	1.693	9.2
o	0	4			[0 0^0 2]					[0 0^0 2]		
			P(3)	1112.82	1.439 (−19)	−8.66	−0.5	/ − 1.4/	1121.486	1.447 (−19)	−0.579	5.7
			P(2)	1119.65	4.324 (−19)	−8.66	−0.7	/ − 1.1/	1128.302	4.354 (−19)	−0.574	4.5
			P(1)	1125.68	5.919 (−19)	−8.66	−0.8	/ − 0.7/	1134.335	5.969 (−19)	−0.569	5.7
			R(0)	1135.37	9.929 (−19)	−8.68	−1.1	/ 0.1/	1144.046	1.004 (−18)	−0.568	6.1
			R(1)	1139.02	1.216 (−18)	−8.70	−1.2	/ 0.5/	1147.716	1.231 (−18)	−0.570	8.5
			R(2)	1141.86	6.774 (−19)	−8.73	−1.3	/ 0.9/	1150.589	6.862 (−19)	−0.575	9.1
			R(3)	1143.90	2.035 (−19)	−8.76	−1.4	/ 1.4/	1152.658	2.063 (−19)	−0.581	12.1
p	0	4			[0 0^0 2]					[0 0^0 2]		
			P(3)	1112.83	7.196 (−20)	−8.66	−0.5	/ − 1.4/	1121.487	7.232 (−20)	−0.579	4.7
			P(2)	1119.65	2.162 (−19)	−8.65	−0.7	/ − 1.0/	1128.304	2.177 (−19)	−0.573	5.5
			P(1)	1125.68	2.960 (−19)	−8.65	−0.8	/ − 0.7/	1134.338	2.984 (−19)	−0.570	4.7
			R(0)	1135.37	4.965 (−19)	−8.67	−1.1	/ 0.1/	1144.049	5.019 (−19)	−0.568	7.2
			R(1)	1139.02	6.080 (−19)	−8.70	−1.2	/ 0.5/	1147.718	6.152 (−19)	−0.570	7.4
			R(2)	1141.87	3.387 (−19)	−8.72	−1.3	/ 1.0/	1150.590	3.431 (−19)	−0.575	10.1
			R(3)	1143.90	1.018 (−19)	−8.76	−1.4	/ 1.4/	1152.658	1.032 (−19)	−0.582	11.1
o	0	5			[1 0^0 0]					[1 0^0 0]		
			P(3)	1300.29	7.491 (−19)	−1.15	−5.0	/ − 6.6/	1301.440	7.883 (−19)	1.185	12.6
			P(2)	1305.75	2.286 (−18)	−1.15	−5.0	/ − 6.4/	1306.908	2.405 (−18)	1.187	13.1
			P(1)	1311.11	3.146 (−18)	−1.16	−5.1	/ − 6.2/	1312.268	3.314 (−18)	1.189	13.2
			R(0)	1321.48	5.182 (−18)	−1.18	−5.3	/ − 6.0/	1322.653	5.474 (−18)	1.192	13.9
			R(1)	1326.49	6.198 (−18)	−1.18	−5.5	/ − 6.0/	1327.670	6.563 (−18)	1.194	13.9
			R(2)	1331.37	3.344 (−18)	−1.19	−5.8	/ − 6.0/	1332.563	3.550 (−18)	1.194	14.2
			R(3)	1336.11	9.644 (−19)	−1.21	−6.1	/ − 6.1/	1337.322	1.027 (−18)	1.194	14.1
p	0	5			[1 0^0 0]					[1 0^0 0]		
			P(3)	1300.32	3.752 (−19)	−1.14	−4.9	/ − 6.5/	1301.461	3.946 (−19)	1.185	12.8
			P(2)	1305.80	1.145 (−18)	−1.14	−4.9	/ − 6.3/	1306.943	1.204 (−18)	1.188	12.9
			P(1)	1311.16	1.576 (−18)	−1.15	−5.0	/ − 6.1/	1312.311	1.659 (−18)	1.189	13.4
			R(0)	1321.52	2.597 (−18)	−1.17	−5.2	/ − 5.9/	1322.688	2.740 (−18)	1.193	13.7
			R(1)	1326.51	3.106 (−18)	−1.18	−5.5	/ − 5.9/	1327.692	3.285 (−18)	1.194	14.0
			R(2)	1331.37	1.675 (−18)	−1.20	−5.7	/ − 6.0/	1332.568	1.777 (−18)	1.194	14.0
			R(3)	1336.09	4.827 (−19)	−1.22	−6.1	/ − 6.1/	1337.312	5.139 (−19)	1.193	14.3
o	0	6			[0 2^0 1]					[0 2^0 1]^b ?		
			P(3)	1353.36	5.935 (−20)	−4.90	67.2	/60.5/	1358.261	3.549 (−20)	0.670	−41.4
			P(2)	1359.66	1.740 (−19)	−4.91	67.6	/61.0/	1364.573	1.038 (−19)	0.678	−43.4
			P(1)	1365.43	2.357 (−19)	−4.92	67.7	/61.2/	1370.349	1.406 (−19)	0.683	−43.7
			R(0)	1375.39	4.028 (−19)	−4.93	66.7	/60.8/	1380.318	2.416 (−19)	0.683	−42.9
			R(1)	1379.56	5.078 (−19)	−4.93	65.8	/60.2/	1384.492	3.063 (−19)	0.678	−40.4
			R(2)	1383.16	2.943 (−19)	−4.93	64.3	/59.4/	1388.088	1.791 (−19)	0.671	−37.9
			R(3)	1386.15	9.249 (−20)	−4.91	62.0	/57.6/	1391.070	5.711 (−20)	0.663	−33.8
p	0	6			[0 2^0 1]					[0 2^0 1]^b ?		
			P(3)	1353.65	2.917 (−20)	−4.90	67.4	/60.5/	1358.542	1.742 (−20)	0.671	−42.5
			P(2)	1360.06	8.512 (−20)	−4.90	67.9	/61.2/	1364.961	5.070 (−20)	0.680	−43.8
			P(1)	1365.89	1.149 (−19)	−4.91	67.9	/61.4/	1370.792	6.842 (−20)	0.686	−45.0
			R(0)	1375.79	1.969 (−19)	−4.92	67.0	/61.1/	1380.706	1.179 (−19)	0.685	−43.1
			R(1)	1379.84	2.495 (−19)	−4.93	66.0	/60.6/	1384.773	1.503 (−19)	0.680	−41.3
			R(2)	1383.30	1.454 (−19)	−4.93	64.3	/59.6/	1388.229	8.848 (−20)	0.672	−37.7
			R(3)	1386.15	4.580 (−20)	−4.91	61.3	/57.2/	1391.063	2.840 (−20)	0.664	−34.1
o	1	4			[0 1^1 2]					[0 1^1 2]^b		
			P(3)	1430.58	5.454 (−21)	−11.04	13.7	/ 62.5/	1441.623	4.796 (−21)	−0.473	5.0
			P(2)	1438.08	5.760 (−21)	−11.05	11.5	/ 86.7/	1449.129	5.167 (−21)	−0.471	26.2
			R(0)	1453.81	8.159 (−21)	−11.07	40.4	/ − 92.6/	1464.874	5.809 (−21)	−0.466	−96.1
			R(1)	1456.78	3.588 (−20)	−11.08	27.5	/ − 45.8/	1467.854	2.815 (−20)	−0.465	−85.9
			R(2)	1458.64	4.236 (−20)	−11.08	23.7	/ − 24.7/	1469.721	3.424 (−20)	−0.463	−70.9
			R(3)	1459.44	2.181 (−20)	−11.06	21.8	/ − 13.3/	1470.504	1.791 (−20)	−0.458	−59.8

TABLE FVII. continued

p	1	4			$[0\,1^1\,2]$					$[0\,1^1\,2]^b$		
			P(3)	1430.42	2.671 (−21)	−11.04	14.0	/ 63.5/	1441.463	2.343 (−21)	−0.473	2.9
			P(2)	1437.76	2.814 (−21)	−11.06	12.1	/ 88.9/	1448.819	2.511 (−21)	−0.470	26.8
			R(0)	1453.48	3.991 (−21)	−11.08	42.1	/ − 93.2/	1464.564	2.809 (−21)	−0.465	−95.0
			R(1)	1456.62	1.757 (−20)	−11.08	28.1	/ − 46.2/	1467.693	1.372 (−20)	−0.463	−87.3
			R(2)	1458.67	2.090 (−20)	−11.07	24.2	/ − 24.7/	1469.739	1.683 (−20)	−0.461	−71.4
			R(3)	1459.64	1.085 (−20)	−11.04	22.1	/ − 13.1/	1470.684	8.880 (−21)	−0.457	−61.0
o	0	7			$[0\,0^0\,3]$					$[0\,0^0\,3]^b$		
			P(3)	1478.29	1.005 (−19)	−13.92	0.7	/ − 1.2/	1492.214	9.985 (−20)	−1.063	−38.9
			P(2)	1485.90	3.105 (−19)	−13.95	0.7	/ − 0.3/	1499.843	3.083 (−19)	−1.067	−40.1
			P(1)	1492.32	4.312 (−19)	−13.96	0.7	/ 0.5/	1506.285	4.284 (−19)	−1.067	−39.1
			R(0)	1501.62	7.165 (−19)	−13.97	0.3	/ 1.8/	1515.588	7.144 (−19)	−1.062	−38.1
			R(1)	1504.49	8.564 (−19)	−13.96	0.0	/ 2.3/	1518.445	8.565 (−19)	−1.055	−35.5
			R(2)	1506.17	4.593 (−19)	−13.94	−0.4	/ 2.8/	1520.108	4.614 (−19)	−1.045	−34.0
			R(3)	1506.69	1.308 (−19)	−13.90	−1.0	/ 3.2/	1520.587	1.322 (−19)	−1.032	−30.2
p	0	7			$[0\,0^0\,3]$					$[0\,0^0\,3]^b$		
			P(3)	1478.35	5.037 (−20)	−13.92	0.7	/ − 1.1/	1492.268	5.001 (−20)	−1.065	−39.8
			P(2)	1485.99	1.555 (−19)	−13.94	0.8	/ − 0.3/	1499.927	1.543 (−19)	−1.069	−39.3
			P(1)	1492.43	2.158 (−19)	−13.95	0.7	/ 0.5/	1506.385	2.143 (−19)	−1.069	−40.0
			R(0)	1501.71	3.587 (−19)	−13.96	0.4	/ 1.8/	1515.671	3.575 (−19)	−1.063	−37.3
			R(1)	1504.55	4.290 (−19)	−13.95	0.0	/ 2.4/	1518.499	4.289 (−19)	−1.056	−36.4
			R(2)	1506.19	2.302 (−19)	−13.94	−0.4	/ 2.8/	1520.128	2.311 (−19)	−1.046	−33.2
			R(3)	1506.67	6.555 (−20)	−13.90	−1.0	/ 3.2/	1520.577	6.623 (−20)	−1.033	−31.0
o	1	6			$[0\,1^1\,3]$					$[0\,1^1\,3]^b$		
			P(3)	1705.16	7.163 (−21)	−16.31	18.4	/ 50.7/	1721.469	6.049 (−21)	−0.945	−62.6
			P(2)	1715.70	1.188 (−20)	−16.38	32.2	/ 82.1/	1732.080	8.990 (−21)	−0.966	−58.0
			R(3)	1722.78	1.301 (−20)	−14.84	21.5	/ − 5.7/	1737.625	1.071 (−20)	−0.594	−85.6
			R(2)	1727.60	3.854 (−20)	−14.89	54.7	/ 13.4/	1742.493	2.490 (−20)	−0.533	−87.6
			R(1)	1731.36	6.384 (−20)	−16.34	24.7	/ − 16.0/	1747.699	5.121 (−20)	−0.936	−91.6
			R(0)	1731.42	2.889 (−20)	−16.40	44.2	/ − 34.8/	1747.825	2.004 (−20)	−0.961	−98.8
p	1	6			$[0\,1^1\,3]$					$[0\,1^1\,3]^b$		
			P(3)	1708.07	1.903 (−21)	−14.65	12.3	/ 44.6/	1722.714	1.694 (−21)	−0.694	−73.7
			P(2)	1711.06	2.403 (−21)	−16.18	26.6	/ 119.8/	1727.239	1.899 (−21)	−0.870	−69.8
			R(0)	1726.78	7.350 (−21)	−16.20	43.1	/ − 71.6/	1742.984	5.137 (−21)	−0.865	−88.8
			R(1)	1734.26	1.759 (−20)	−14.68	16.1	/ − 23.7/	1748.945	1.516 (−20)	−0.685	−97.8
			R(2)	1738.12	1.542 (−20)	−14.02	5.9	/ − 7.4/	1752.137	1.456 (−20)	−0.561	−85.4
			R(3)	1739.02	5.457 (−21)	−13.58	−3.0	/ − 3.9/	1752.598	5.625 (−21)	−0.427	−73.2
o	0	10			$[0\,0^0\,4]$					$[0\,0^0\,4]^b$		
			P(3)	1721.33	1.539 (−20)	−17.55	−6.3	/ − 18.6/	1738.875	1.643 (−20)	−1.194	−89.9
			P(2)	1727.90	5.653 (−20)	−17.95	−3.5	/ − 10.3/	1745.847	5.855 (−20)	−1.259	−88.8
			P(1)	1733.37	9.304 (−20)	−18.31	1.3	/ 2.1/	1751.681	9.187 (−20)	−1.308	−85.7
			R(0)	1743.62	1.252 (−19)	−17.97	−5.5	/ 11.5/	1761.592	1.325 (−19)	−1.254	−81.8
			R(1)	1747.52	1.214 (−19)	−17.58	−9.5	/ 12.9/	1765.106	1.342 (−19)	−1.186	−78.8
			R(2)	1750.25	4.950 (−20)	−17.02	−17.2	/ 10.2/	1767.264	5.976 (−20)	−1.088	−76.3
			R(3)	1752.13	9.184 (−21)	−16.02	−31.2	/ − 1.0/	1768.149	1.334 (−20)	−0.905	−70.1
p	0	10			$[0\,0^0\,4]$					$[0\,0^0\,4]^b$		
			P(3)	1722.88	9.352 (−21)	−17.84	−6.3	/ − 13.9/	1740.720	9.986 (−21)	−1.211	−76.1
			P(2)	1730.26	3.398 (−20)	−18.16	−1.7	/ − 5.0/	1748.419	3.457 (−20)	−1.278	−76.3
			P(1)	1736.70	4.983 (−20)	−18.29	−0.4	/ 0.5/	1754.984	5.001 (−20)	−1.307	−76.9
			R(0)	1745.98	7.644 (−20)	−18.18	−2.9	/ 6.7/	1764.164	7.873 (−20)	−1.273	−70.7
			R(1)	1749.08	7.642 (−20)	−17.87	−8.4	/ 6.0/	1766.951	8.344 (−20)	−1.202	−66.1
			R(2)	1751.47	2.952 (−20)	−17.31	−17.8	/ 1.1/	1768.784	3.589 (−20)	−1.096	−58.0
			R(3)	1752.96	5.458 (−21)	−16.59	−27.7	/ − 5.1/	1769.545	7.547 (−21)	−0.963	−52.0

TABLE FVII. continued

o	1	7			$[1\,1^1\,0]$					$[1\,1^1\,0]^b$		
			P(3)	1804.77	1.741 (−21)	0.98	27.0	/ − 75.8/	1803.791	1.371 (−21)	1.214	−89.5
			P(2)	1809.95	4.278 (−21)	0.39	37.5	/ − 71.5/	1809.556	3.110 (−21)	1.290	−81.5
			Q(3)	1820.37	5.615 (−21)	1.99	56.9	/ − 58.2/	1818.376	3.578 (−21)	0.833	−61.4
			Q(1)	1820.49	3.253 (−20)	0.40	38.5	/ − 62.8/	1820.094	2.349 (−20)	1.293	−56.2
			Q(2)	1820.67	1.803 (−20)	1.01	29.5	/ − 65.2/	1819.657	1.392 (−20)	1.213	−56.7
			R(0)	1825.67	3.425 (−20)	0.37	39.3	/ − 57.5/	1825.301	2.460 (−20)	1.295	−38.1
			R(1)	1830.97	2.703 (−20)	0.95	30.7	/ − 56.2/	1830.022	2.068 (−20)	1.222	−18.2
			R(2)	1835.71	1.298 (−20)	1.81	60.8	/ − 44.4/	1833.904	8.074 (−21)	0.878	6.6
			R(3)	1840.03	2.810 (−21)	−1.85	47.2	/ − 16.4/	1841.876	1.909 (−21)	0.895	−16.8
p	1	8			$[1\,1^1\,0]$					$[1\,1^1\,0]^b$		
			P(3)	1810.44	7.294 (−22)	−0.42	91.5	/ − 30.5/	1810.865	3.808 (−22)	1.254	107.1
			P(2)	1816.66	1.606 (−21)	−0.47	83.2	/ − 31.2/	1817.130	8.769 (−22)	1.251	47.0
			Q(3)	1826.11	2.694 (−21)	−0.40	47.4	/ − 50.1/	1826.506	1.827 (−21)	1.279	−53.5
			Q(2)	1826.91	8.653 (−21)	−0.37	53.3	/ − 49.7/	1827.281	5.643 (−21)	1.272	−53.9
			Q(1)	1827.38	1.399 (−20)	−0.47	57.0	/ − 49.0/	1827.851	8.910 (−21)	1.258	−54.0
			R(0)	1832.38	1.591 (−20)	−0.49	45.9	/ − 56.2/	1832.875	1.091 (−20)	1.256	−80.0
			R(1)	1836.64	1.467 (−20)	−0.46	32.7	/ − 60.0/	1837.096	1.106 (−20)	1.263	−92.9
			R(2)	1840.19	6.628 (−21)	−0.67	14.8	/ − 57.3/	1840.862	5.773 (−21)	1.255	−98.2
			R(3)	1841.84	1.007 (−21)	−2.28	−36.0	/ − 41.3/	1844.123	1.575 (−21)	1.195	−100.0
o	0	13			$[0\,0^0\,5]$					$[0\,0^0\,5]^b$		
			P(3)	1852.67	4.249 (−21)	−22.67	14.7	/ 2.8/	1875.333	3.705 (−21)	−1.110	−69.7
			P(2)	1864.16	1.329 (−20)	−22.49	−2.6	/ − 7.8/	1886.652	1.365 (−20)	−1.269	−90.9
			R(3)	1869.43	2.892 (−21)	−19.98	−9.3	/ − 2.7/	1889.409	3.190 (−21)	−0.883	−91.3
			P(1)	1872.67	1.837 (−20)	−22.45	−5.3	/ 3.2/	1895.121	1.940 (−20)	−1.317	−94.7
			R(2)	1875.21	1.308 (−20)	−23.59	35.6	/ 12.6/	1898.803	9.651 (−21)	−0.792	−30.9
			R(1)	1878.86	2.817 (−20)	−22.70	−12.0	/ 84.7/	1901.564	3.200 (−20)	−1.102	−78.9
			R(0)	1879.89	2.608 (−20)	−22.51	−15.2	/ 37.5/	1902.397	3.074 (−20)	−1.264	−92.5
p	0	12			$[0\,0^0\,4]$					$[0\,0^0\,4]^b$?		
			P(3)	1862.39	2.699 (−21)	−17.27	22.8	/ 21.2/	1879.661	2.198 (−21)	−0.694	−76.7
			P(2)	1872.26	8.106 (−21)	−17.30	35.7	/ 35.2/	1889.551	5.975 (−21)	−0.710	−91.3
			P(1)	1879.81	1.104 (−20)	−17.34	40.8	/ 39.2/	1897.145	7.842 (−21)	−0.732	−97.4
			R(3)	1882.65	2.640 (−21)	−17.33	−23.6	/ 26.6/	1899.977	3.456 (−21)	−0.671	−1.1
			R(2)	1886.83	1.136 (−20)	−17.31	−4.2	/ 15.0/	1904.137	1.185 (−20)	−0.676	−51.7
			R(0)	1887.98	1.877 (−20)	−17.32	29.4	/ 3.2/	1905.296	1.451 (−20)	−0.705	−93.5
			R(1)	1888.58	2.252 (−20)	−17.31	14.3	/ − 5.5/	1905.892	1.970 (−20)	−0.685	−81.5
o	1				$[1\,0^0\,1]$							
			P(3)	2010.5	1.74 (−20)^c							
			P(2)	2016.9	5.68 (−20)							
			P(1)	2023.3	7.92 (−20)							
			R(0)	2032.6	1.28 (−19)							
			R(1)	2036.7	1.44 (−19)							
			R(2)	2041.5	1.06 (−19)							
			R(3)	2045.9	3.48 (−20)							
p	1				$[1\,0^0\,1]$							
			P(3)	2013.2	8.22 (−21)^c							
			P(2)	2021.1	2.18 (−20)							
			P(1)	2027.9	2.68 (−20)							
			R(0)	2036.7	5.01 (−20)							
			R(1)	2039.4	6.08 (−20)							
			R(2)	2041.7	5.01 (−20)							
			R(3)	2043.3	1.32 (−20)							

$^\natural$ The similarity of these deviations with the δIs in column 'D^{2}FOPI vs CCVM', especially in the perpendicular bands $[0\,0^0\,0]\rightarrow[0\,1^1\,0]$, $\rightarrow[1\,1^1\,0]$, suggest the following explanation for the surprisingly large size of the latter: the dipole moment data used in calculations with the D^{2}FOPI method was actually not exactly the same as used in the CCVM calculations. In particular, the component d_X appears not included.
^{a},^{b},^{c} See the respective footnote to Table FVI.

Natural Expansion Analysis[16]

in application to

ro-vibrational bound state functions of atom-diatom complexes

determined in

the CC-BF approach[17]

(Jacobi coordinates in body-fixed reference frame,
close-coupling in diabatic basis)

The functions have the form

$$\Psi^{JMp}(E^{\rm B};\mathbf{r},\mathbf{R}) \;=\; \sum_{\lambda=(1-p)/2}^{J} \Psi^{Jp}_{\lambda}(E^{\rm B};r,R,\theta)\,\Theta^{JMp}_{\lambda}(\alpha,\beta,\gamma)\,, \tag{F3}$$

$$\Theta^{JMp}_{\lambda}(\alpha,\beta,\gamma) \;=\; \left[\tfrac{2J+1}{16\pi^2(1+\delta_{\lambda,0})}\right]^{\frac{1}{2}}[D^{J*}_{M,\lambda}(\alpha,\beta,\gamma)+p(-1)^{\lambda}D^{J*}_{M,-\lambda}(\alpha,\beta,\gamma)]\,, \tag{F4}$$

$$\Psi^{Jp}_{\lambda}(E^{\rm B};r,R,\theta) \;=\; \frac{1}{rR}\sum_{v}\sum_{j(\le\lambda)} F^{Jp}_{v,j,\lambda}(E^{\rm B};R)\,\chi_{v,j}(r)\,\tau_{j,\lambda}(\theta)\,, \tag{F5}$$

where $\mathbf{r}$, $\mathbf{R}$ — the Jacobi vectors of the system, the latter joining the diatomic center-of-mass with the atom, θ — the angle between the vectors, α,β,γ — the Euler angles of rotation from the SF to BF reference frame with z-axis along $\mathbf{R}$ and y-axis perpendicular to the three atom plane,
J, M, λ — the quantum numbers of the total angular momentum and its projections on the SF and the BF z-axes, $p\,(=1,-1\,\text{or}\,e,f)$ — the spectroscopic parity, $E^{\rm B}$ — the energy of a given state,
$D^{J}_{M,\lambda}(\alpha,\beta,\gamma)$ — the Wigner rotation matrix, thus

$$\int_0^{2\pi}\!d\alpha\int_0^{2\pi}\!d\gamma\int_0^{\pi}\!\sin\beta d\beta\,\Theta^{JMp*}_{\lambda'}(\alpha,\beta,\gamma)\,\Theta^{JMp}_{\lambda}(\alpha,\beta,\gamma)=\delta_{\lambda,\lambda'}\,,$$

$\tau_{j,\lambda}(\theta)$ — function proportional to the reduced rotation matrix $d^{j}_{\lambda,0}(\theta)$ so that

$$\int_0^{\pi}\tau_{j,\lambda}(\theta)\tau_{j',\lambda}(\theta)\,\sin\theta d\theta=\delta_{j,j'}\,,$$

$\chi_{v,j}(r)$ — the vibrational function of the diatom in its vibration-rotation state $|vj\rangle$,

$$\int_0^{\infty}\chi_{v,j}(r)\chi_{v',j}(r)\,dr{=}\delta_{v,v'}\,,$$

$F^{Jp}_{v,j,\lambda}(E^{\rm B};R)$ — the component of the solution of the coupled equations for the atom-diatom vibrations in the state.

The natural expansion — construction

$$\Psi^{Jp}_{\lambda}(E^{\rm B};r,R,\theta)=\frac{1}{rR}\sum_{i}\sum_{m}\sqrt{a^{\lambda}_{i}}\sqrt{c^{\lambda}_{i,m}}\,h^{\lambda}_{i}(r)\,f^{\lambda}_{i,m}(R)\,t^{\lambda}_{i,m}(\theta)\,, \tag{F6}$$

where $h^{\lambda}_{i}(r)$, $f^{\lambda}_{i,m}(R)$, and $t^{\lambda}_{i,m}(\theta)$ — the natural orbitals — are eigenfunctions of 1-dim. reduced density kernels $\rho_{\lambda}(r,r')$, $\rho^{\lambda}_{i}(R,R')$, and $\rho^{\lambda}(\theta,\theta')$, respectively, defined as follows

$$\rho_{\lambda}(r,r') \;=\; rr'\int_0^{\infty}R^2dR\int_0^{\pi}\sin\theta d\theta\,\Psi_{\lambda}(r,R,\theta)\Psi_{\lambda}(r',R,\theta) \tag{F7}$$

$$\;=\; \sum_{v}\sum_{v'}\sum_{j}\chi_{v,j}(r)\,Z^{\lambda}_{v,j;v',j}\,\chi_{v',j}(r') \tag{F8}$$

$$\;=\; \sum_{i}h^{\lambda}_{i}(r)\,a^{\lambda}_{i}\,h^{\lambda}_{i}(r')\,,\qquad \int_0^{\infty}h^{\lambda}_{i}(r)h^{\lambda}_{i'}(r)dr=\delta_{i,i'}\,, \tag{F9}$$

where

$$Z^{\lambda}_{v,j;v',j'}:=\int_0^{\infty}F_{v,j,\lambda}(R)\,F_{v',j'\lambda}(R)\,,dR$$

(the symbols J, p and $E^{\rm B}$ are hereafter omitted),

$$\rho_i^\lambda(R,R') \;=\; \int_0^\pi \psi_i^\lambda(R,\theta)\,\psi_i^\lambda(R',\theta)\,\sin\theta d\theta\,, \tag{F10}$$

$$\rho_i^\lambda(\theta,\theta') \;=\; \int_0^\infty \psi_i^\lambda(R,\theta)\,\psi_i^\lambda(R,\theta')\,R^2 dR\,, \tag{F11}$$

where the functions $\psi_i^\lambda(R,\theta)$ come from the expansion implied by Eqs. (F7) and (F9):

$$\Psi_\lambda(r,R,\theta) = \frac{1}{r}\sum_i \sqrt{a_i^\lambda}\,h_i^\lambda(r)\,\psi_i^\lambda(R,\theta)\,. \tag{F12}$$

Thus,

$$\rho_i^\lambda(R,R') \;=\; \sum_v \sum_{v'} \sum_j z^\lambda_{v,j;i}\,F_{v,j,\lambda}(R)\,F_{v',j,\lambda}(R')\,z^\lambda_{v',j;i}\,, \tag{F13}$$

$$\rho_i^\lambda(\theta,\theta') \;=\; \sum_v \sum_j \sum_{v'} \sum_{j'} \tau_{j,\lambda}(\theta)\,z^\lambda_{v,j;i}\,Z^\lambda_{v,j;v',j'}\,z^\lambda_{v',j';i}\,\tau_{j',\lambda}(\theta')\,, \tag{F14}$$

where

$$z^\lambda_{v,j;i} := \frac{1}{\sqrt{a_i^\lambda}}\int_0^\infty \chi_{v,j}(r)\,h_i^\lambda(r)\,dr\,.$$

The kernels $\rho_i^\lambda(R,R')$ and $\rho_i^\lambda(\theta,\theta')$ have common eigenvalues,

$$\int_0^\infty \rho_i^\lambda(R,R')\,f^\lambda_{i,m}(R')\,dR' = c^\lambda_{i,m} f^\lambda_{i,m}(R)\,, \tag{F15}$$

$$\int_0^\infty \rho_i^\lambda(\theta,\theta')\,t^\lambda_{i,m}(\theta')\,\sin\theta' d\theta' = c^\lambda_{i,m} t^\lambda_{i,m}(\theta)\,, \tag{F16}$$

and their eigenfunctions satisfy the orthonormality relations

$$\int_0^\infty f^\lambda_{i,m}(R) f^\lambda_{i,m'}(R)\,dR = \delta_{m,m'}\,, \tag{F17}$$

$$\int_0^\pi t^\lambda_{i,m}(\theta)\,t^\lambda_{i,m'}(\theta)\,\sin\theta\,d\theta = \delta_{m,m'}\,. \tag{F18}$$

The traces of the three 1-dim density kernels are:

$$\int_0^\infty \rho_\lambda(r,r)\,dr = \sum_i a_i^\lambda = \rho_\lambda\,, \qquad \sum_\lambda \rho_\lambda = 1\,, \tag{F19}$$

$$\int_0^\infty \rho_i^\lambda(R,R)\,dR = \int_0^\pi \rho_i^\lambda(\theta,\theta)\,\sin\theta d\theta = \sum_m c^\lambda_{i,m} = 1 \quad \text{for each } i \text{ and } \lambda\,. \tag{F20}$$

The trace of the 3-dim density kernel

$$\rho(r,R,\theta;r',R',\theta') = \sum_\lambda \Psi_\lambda(r,R,\theta)\Psi_\lambda(r',R',\theta') \tag{F21}$$

is:

$$\int_0^\infty r^2 dr \int_0^\infty R^2 dR \int_0^\pi \sin\theta d\theta\,\rho(r,R,\theta;r,R,\theta) = \sum_\lambda \sum_i \sum_m a_i^\lambda c^\lambda_{i,m} = 1\,. \tag{F22}$$

Hence, the number $a_i^\lambda c^\lambda_{i,m}$ gives the occupancy of the natural configuration $h_i^\lambda(r)\,f^\lambda_{i,m}(R)\,t^\lambda_{i,m}(\theta)$ in the considered bound state function.

If the orbitals $h_i^\lambda(r)$, $f_{i,m}^\lambda(R)$, and $t_{i,m}^\lambda(\theta)$ have clear nodal structures, quantum numbers can be assigned to them as characteristics of motions in their respective coordinates. The numbers v_r, v_R, and v_θ are defined as equal to the numbers of nodes in the orbitals.

A comment should be added as to the quantum number for the θ motion. All nodes inside the range $[0,\pi]$ are counted in the number v_θ. This definition is appropriate for atom-diatom complexes formed on the PESs $\overline{V}(r,R,\theta)$ whose anisotropy is dominated by the $V_{L=2}(r,R)P_2(\cos\theta)$ term with the strength $V_{L=2}(r,R)>0$ (T-shape equilibrium geometry)[6]. However, for complexes with large negative L=2 anisotropy (linear equilibrium geometry, large barrier at T-geometry), it is more convenient to use a slightly modified number $\widetilde{v}_\theta$ in which the node at $\theta=\frac{\pi}{2}$ in the antisymmetric orbitals, $t_{i,m}^\lambda(\theta)=-t_{i,m}^\lambda(\pi-\theta)$ is not counted. The sum $\widetilde{v}_\theta+\lambda\,(:=v_b)$ correlates with the vibrational number of circular harmonic oscillator.

For given λ, the eigenvalues a_i^λ are ranged in descending order, $a_1^\lambda>a_2^\lambda>\ldots$, and analogously are ranged the eigenvalues $c_{i,m}^\lambda$ for given λ and i: $c_{i,1}^\lambda>c_{i,2}^\lambda\ldots$. If among λ values admissible for given J and p, there exists clearly dominant configuration $h_1^\lambda(r)\,f_{1,1}^\lambda(R)\,t_{1,1}^\lambda(\theta)$, with the occupancy $a_1^\lambda c_{1,1}^\lambda\times100\%$ greater than 70 %, say, then the pertaining quantum numbers v_r, v_θ (or $\widetilde{v}_\theta$), and v_R may be considered ascribable together with the λ (denoted by k) to the entire bound state function, Eq. (F3). Obviously, the existence of dominant ρ_λ value, cf. Eq. (F19), suffices for ascribing only the number k to the function.

Fig. F6. NEA. Illustrative examples

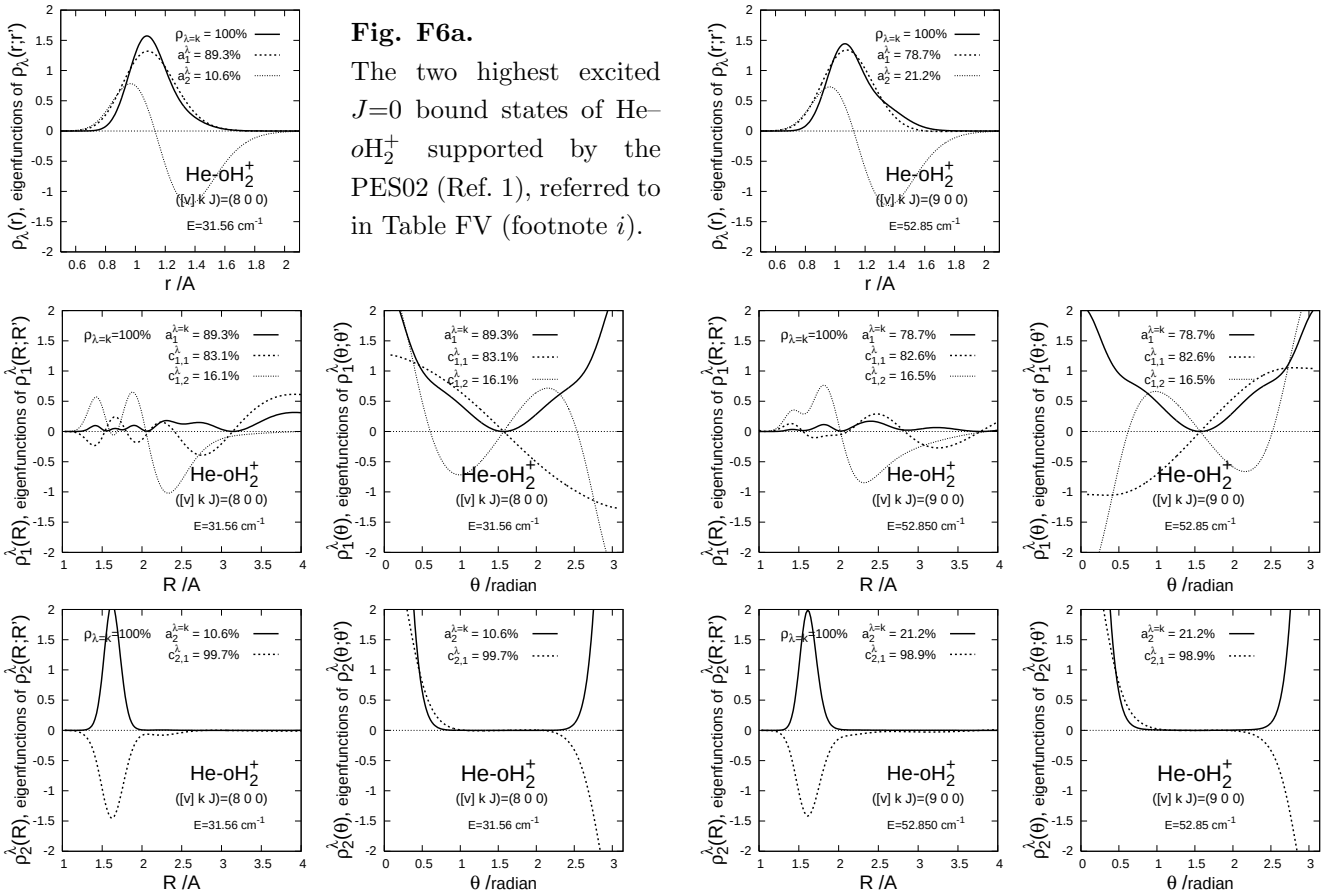

Fig. F6a.
The two highest excited J=0 bound states of He–oH$_2^+$ supported by the PES02 (Ref. 1), referred to in Table FV (footnote i).

$[v_r\;\widetilde{v}_\theta\;v_R]$=[0 0 5] with $a_1^0c_{1,1}^0$=74.2% — the most populated, and [1 0 0] with $a_2^0c_{2,1}^0$=10.6% — the third most populated configuration in the state $([v]\,k\,J)$=(8 0 0).

[1 0 0] with $a_2^0c_{2,1}^0$=21.0% is the second most populated configuration in state $([v]\,k\,J)$=(9 0 0) — the fact overlooked in Ref. 3 /since configurations containing the highest populated orbital in the r-coordinate (with a_1^λ) were only analyzed/.

Fig. F6b.
One of the states referred to in Table FV (footnote *p*), observed in the experiment reported in Ref. 5 but difficult to assign on the basis of calculations performed there.

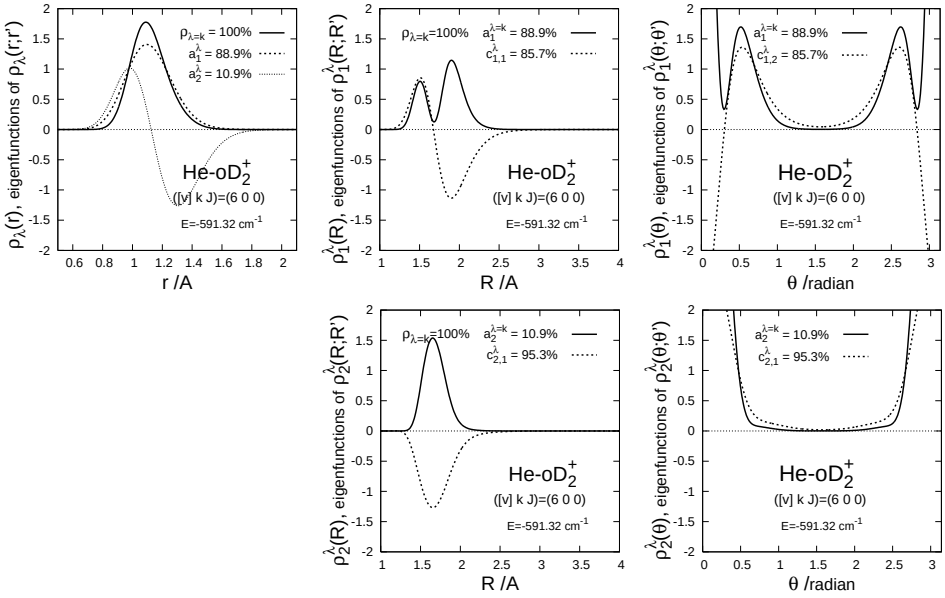

Fig. F5c. States which may be assigned with $[v_r\ v_b^k\ v_R]$=$[1\,1^1\,0]$ with v_b=$\widetilde{v}_\theta$+k.

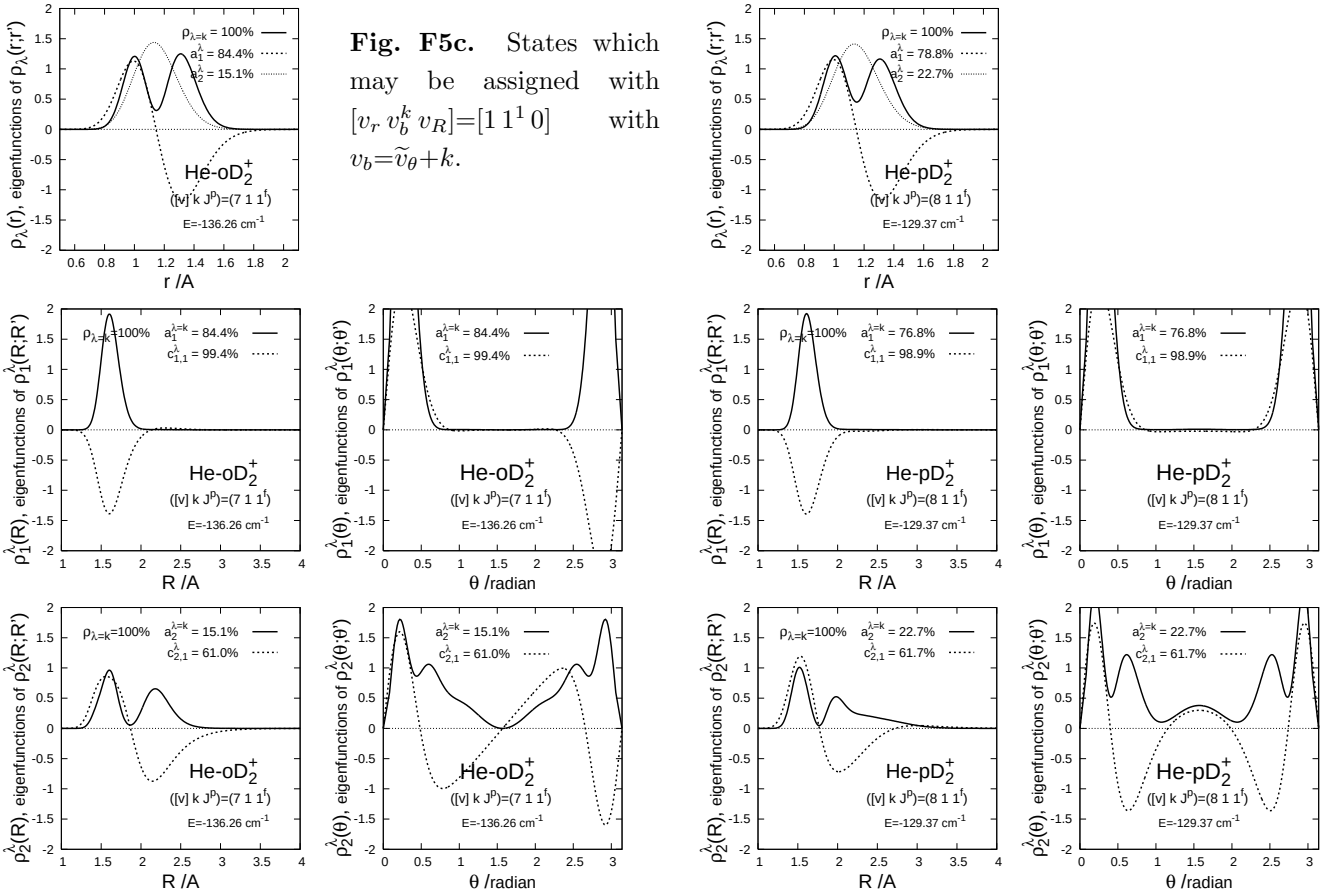

In the labels of the vertical axes: $\rho_\lambda(r)$, $\rho_i^\lambda(R)$, and $\rho_i^\lambda(\theta)$ denote the diagonal elements of the respective density kernels, $\rho_\lambda(r,r')$, $\rho_i^\lambda(R,R')$, and $\rho_i^\lambda(\theta,\theta')$. The density kernels in the radial coordinates are ploted in the unit of bohr^{-1}, their egenfunctions — in bohr$^{-\frac{1}{2}}$.

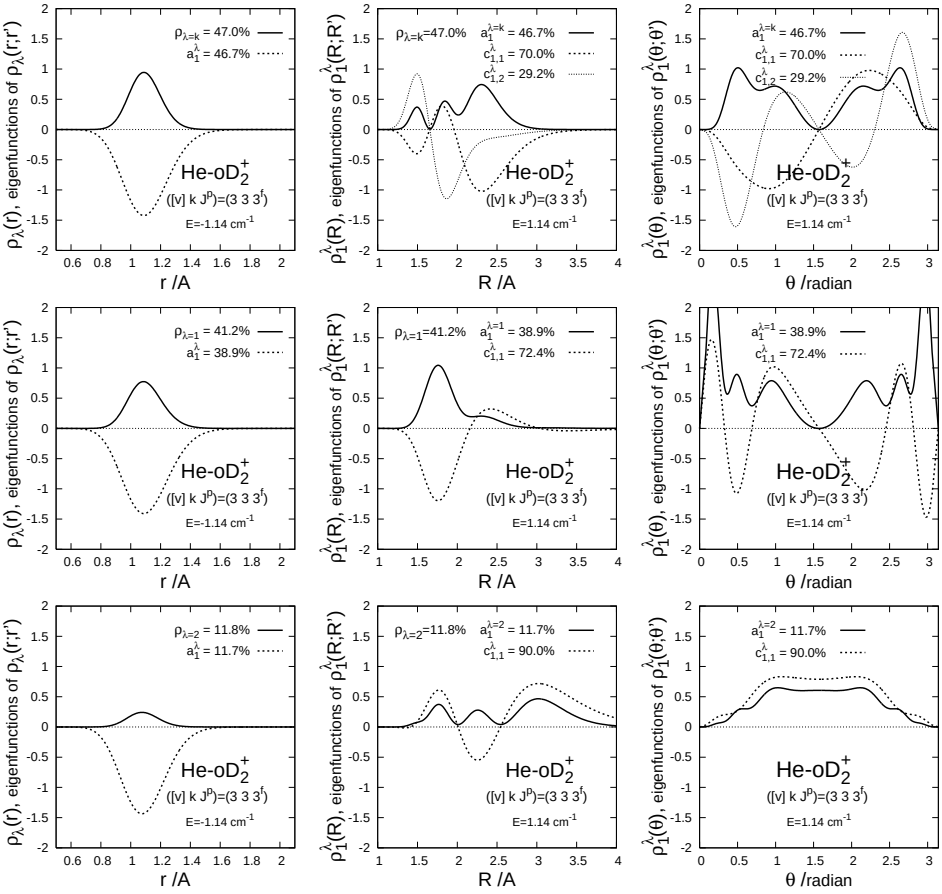

Fig. F5d. An example of state with heavy λ-mixing, unassignable: no natural configuration populated in more than 50% exists.

[1] W. P. Kraemer, V.Špirko, and O. Bludsky, Chem. Phys. **276**, 225 (2002).
[2] M. Juřek, V. Špirko, and W. P. Kraemer, J. Mol. Spectrosc. **182**, 364 (1997).
[3] F. Mrugała and W. P. Kraemer, J. Chem. Phys. **122**, 224321 (2005).
[4] D. Koner, J.C.S.V. Veliz, A. van der Avoird, and M. Meuwly, Phys. Chem. Chem. Phys.**21**, 24976 (2019).
[5] O. Asvany, S. Schlemmer, Ad van der Avoird, and T. Szidarovszky, A. G. Császár, J. Mol. Spectrosc. **377**, 111423 (2021).
[6] J.M. Hutson, Adv. Mol. Vib. Collision Dyn. **1A**, 1 (1991).
[7] F. Mrugała and W. P. Kraemer, J. Chem. Phys. **138**, 104315 (2013).
[8] A. J. Page and E. I. von Nagy-Felsobuki, J. Phys. Chem. **A 111**, 4478 (2007).
[9] W.P. Kraemer, M. Juřek, and V. Špirko, J. Mol. Spectrosc. **187**, 206 (1998).
[10] M. Šindelka, V, Špirko, and W. P. Kraemer, Theor. Chem. Acc.**110**, 170 (2003).
[11] F. Mrugała, V. Špirko, and W. P. Kraemer, J. Chem. Phys. **118**, 10547 (2003).
[12] V. Špirko and W. P. Kraemer, J. Mol. Spectrosc. **172**, 265 (1995).
[13] D. De Fazio, M. De Castro-Vitores, A. Aguado, V. Aquilanti, and V. Cavalli, J. Chem. Phys. **137**, 244306 (2012).
[14] D. Papp, A. G. Császár, K. Yamanouchi, and T. Szidarovszky, J. Chem. Teory Comput. **14**, 1523 (2018).
[15] M. Meuwly and J. M. Hutson, J. Chem. Phys. **110**, 3418 (1999).
[16] R. M. Stratt, N. C. Handy, and W. H. Miller, J. Chem. Phys. **71**, 3311 (1979); N. Moiseyev and R. E. Wyatt, Chem. Phys. Lett. **112**, 396 (1986); N. Lipkin, N. Moiseyev, and C. Leforestier, J. Chem. Phys. **98**, 1888 (1993)
[17] The first such application was presented in Ref. 3. The description here is more detailed (formulas for evaluation of the reduced density kernels are added) and illustrated with a more diverse set of examples.